Michael Radl, BSc.

Synthesis and Characterization of Covalent Organic Frameworks in Continuous Flow

MASTER'S THESIS

to achieve the university degree of

Diplom-Ingenieur

Master's degree programme:

Verfahrenstechnik

submitted to

Graz University of Technology

Supervisor

Assoc.Prof. Dipl.-Ing. Dr.techn., Heidrun Gruber-Wölfler

Institute of Process and Particle Engineering

Dipl.-Ing. Michael König

Graz, February 2025

EIDESSTATTLICHE ERKLÄRUNG

Ich erkläre an Eides statt, dass ich die vorliegende Arbeit selbstständig verfasst, andere als die angegebenen Quellen/Hilfsmittel nicht benutzt, und die den benutzten Quellen wörtlich und inhaltlich entnommene Stellen als solche kenntlich gemacht habe.

…… …..…….

Datum Unterschrift

STATUTORY DECLARATION

I declare that I have authored this thesis independently, that I have not used other than the declared sources/resources, and that I have explicitly marked all material which has been quoted either literally or by content from the used sources.

…… …..……..

date signature

Abstract

Covalent Organic Frameworks (COFs) are an emerging class of porous crystalline materials with significant potential for catalysis, gas storage, and drug delivery applications. The synthesis of COFs typically requires stringent experimental conditions, including reactions conducted in a sealed Pyrex tube, an inert atmosphere, and extended reaction times. Although COFs have great potential, scaling up their synthesis remains challenging, mainly due to difficulties in achieving high crystallinity and preserving structural integrity during production.

This thesis focuses on the synthesis and characterization of COFs using a continuous flow approach. The study investigates reaction parameters, including solvent choice, mixing methods and rotational speed. The solvents used are dioxane, acetonitrile, and an acetonitrile imidazole solution.

To investigate the reaction kinetics of the synthesis Raman spectroscopy was used, providing insights into the influence of solvent choice, mixing methods and rotational speed on COF formation. Small-angle X-ray scattering (SAXS) and Brunauer, Emmett and Teller (BET) measurements were employed to evaluate crystallinity and specific surface area of the formed products, respectively.

The results demonstrate that continuous flow COF synthesis presents a viable alternative to batch processing, with specific parameters optimizing process feasibility to a maximum run time with given conditions. Key findings of this work include the identification of optimal solvent systems, the positive impact of ultrasonic mixing on the formed COFS, and the successful implementation of slug flow techniques to mitigate clogging issues. Overall, this work contributes to the advancement of scalable COF synthesis methods, offering a foundation for further development.

Zusammenfassung

Covalent Organic Frameworks (COFs) sind eine neuartige Klasse poröser, kristalliner Materialien mit großem Potenzial für Anwendungen in der Katalyse, Gasspeicherung und Wirkstofffreisetzung. Die Synthese von COFs erfordert in der Regel extreme Versuchsbedingungen, darunter Reaktionen in einem versiegelten Pyrex-Rohr, eine inerte Atmosphäre und lange Reaktionszeiten. Obwohl COFs ein großes Potenzial haben, bleibt die Skalierung ihrer Synthese eine Herausforderung, hauptsächlich aufgrund der Schwierigkeiten, eine hohe Kristallinität zu erreichen und die strukturelle Integrität während der Produktion zu bewahren.

Diese Arbeit beschäftigt sich mit der kontinuierlichen Synthese von COFs und deren Charakterisierung. Insbesondere wurde der Einfluss verschiedener Reaktionsparameter auf die Qualität der erhaltenen COFs untersucht, darunter die Wahl des Lösungsmittels, verschiedene Mischmethoden und die Mischintensität. Als Lösungsmittel kamen Dioxan, Acetonitril und eine Acetonitril-Imidazol-Lösung zum Einsatz.

Mithilfe der Raman-Spektroskopie wurde die Reaktionskinetik analysiert, um den Einfluss des Lösungsmittels und des Mischens auf die COF-Bildung besser zu verstehen. Zur Beurteilung der Kristallinität und der spezifischen Oberfläche wurden Small-angle X-Ray Scattering (SAXS) und Brunauer, Emmett und Teller (BET) Messungen durchgeführt.

Die Ergebnisse zeigen, dass die kontinuierliche Synthese von COFs eine vielversprechende Alternative zur herkömmlichen Batch-Verarbeitung darstellt. Unter bestimmten Bedingungen konnten die kontinuierliche Laufzeit der Versuche bei den gegebenen Bedingungen auf das mögliche Maximum erhöht werden. Zu den wichtigsten Erkenntnissen zählen die Identifizierung optimaler Lösungsmittelsysteme, der positive Einfluss von Ultraschall zur Mischung, sowie die erfolgreiche Anwendung von Slug-Flow-Techniken zur Vermeidung von Verstopfungen im Reaktor. Diese Arbeit leistet damit einen wichtigen Beitrag zur Weiterentwicklung skalierbarer Synthesemethoden für COFs und bietet eine solide Grundlage für zukünftige Entwicklungen in diesem Bereich.

Acknowledgment

I would like to take a moment to express my heartfelt thanks to everyone who supported me throughout this thesis.

First, a big thank you to my working group, the CoSy Pros. You were not only a great help with technical issues but also became friends along the way. Your support, motivation, and open discussions made this time much easier and even enjoyable. I'm truly grateful to have had you by my side.

I'm especially thankful to my supervisor, Heidi Gruber-Wölfler, who always made time for my questions and guided me through each stage of this thesis with her knowledge and advice. Her patience, encouragement, and trust in my abilities motivated me and helped me grow.

I also want to thank my adviser, Michael König, for always being there to offer advice and support whenever I needed it. His expertise, clear guidance, and constructive feedback were essential in completing this work.

Finally, I want to express my deep gratitude to my family and friends. Your understanding, kindness, and constant support helped me stay grounded throughout this journey. Whether it was through encouraging words, timely distractions, or simply being there, you made a huge difference. You reminded me to stay balanced even during stressful times.

Thank you all so much. I couldn't have achieved this without your support.

Table of Content

1. Introduction

Covalent Organic Frameworks (COFs) have garnered significant attention due to their unique properties, including high porosity, tuneable chemical functionalities, and exceptional stability [1]. Since their discovery in 2005 [1], they have shown promising applications in diverse fields, such as gas separation [2], catalysis [3], and energy storage [4]. Despite their potential, the scalable synthesis of COFs remains a major challenge [5], primarily due to the difficulties in achieving high crystallinity and maintaining structural integrity during production. [6]

Traditional batch synthesis methods often suffer from limitations such as lengthy reaction times [7], poor reproducibility [8], and mostly with harsh solvothermal conditions [9]. Continuous flow synthesis has emerged as a promising alternative, offering improved control over reaction parameters, mixing regimes and enhanced scalability. [10] However, challenges such as clogging, optimizing residence times, and maintaining high product quality must be addressed for successful implementation.

This thesis aims to investigate the continuous flow synthesis of COFs, investigating key factors that influence their formation, including solvent systems, reaction kinetics, and mixing efficiency. By utilizing advanced analytical techniques such as Raman spectroscopy, SAXS, and BET, the study seeks to optimize process conditions and evaluate their impact on COF properties. The motivation behind this work lies in the need for a reliable, scalable approach to COF synthesis that can facilitate their integration into real-world applications.

2. Theoretical background

2.1. Covalent Organic Frameworks

Covalent Organic Frameworks (COFs) are porous, crystalline polymers with precisely ordered and highly customizable architectures formed from organic building blocks. First reported in 2005 [1], COFs have rapidly gained widespread interest. [6] They are classified into two main types: 2D COFs, which consist of stacked planar layers connected by weak interlayer forces [11], and 3D COFs, which have more complex, non-planar geometries that create intricate microporous structures. However, the limited diversity of 3D building blocks and the difficulty of obtaining high crystallinity have restricted the growth of 3D COF research [12]. The modular design of COFs allows fine-tuning of pore size, shape, and chemical functionality by carefully choosing the building units and linkages, using dynamic covalent chemistry (DCC) to form strong, thermodynamically stable networks. [13] Typically, COFs are synthesized through solvothermal methods [9] involving reversible reactions such as azine [14], triazine [15], hydrazone [16], imine [17], or boronic acid condensation. [1] Figure 1 shows the reaction equation of the earliest COF reaction with a diboronic acid condensation. [1] Alternative approaches offer scalable and efficient production options, including mechanochemical synthesis [18] and microwave-assisted [19] techniques. Thanks to their versatility and tunability, COFs are highly adaptable for numerous applications like drug delivery [20], energy storage [4], optical materials [21], separations [2], and catalysis. [3]

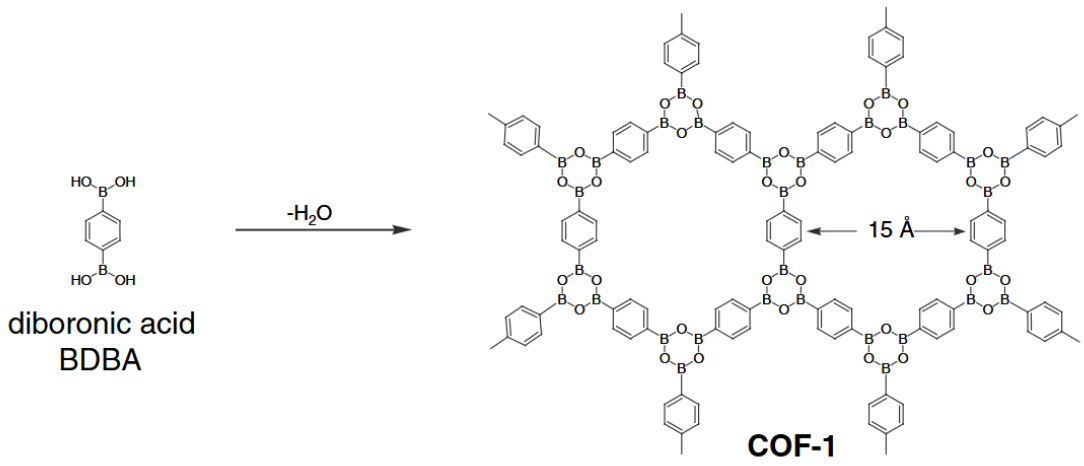

Figure 1: COF-1 as result of a diboronic acid condensation [1]

2.1.1. Topology

Designing the topology of covalent organic frameworks (COFs) is crucial, serving as a blueprint that dictates the overall structure and bonding connections [12]. Monomers, the fundamental building blocks of COFs, have fixed reaction points and rigid shapes. Imagine them as unique puzzle pieces with specific configurations. Representing these monomers with simple geometric shapes helps visualize how they connect through covalent bonds. The bond angles determine the placement of subsequent components, creating a highly ordered, brick-like arrangement. [22] A wide variety of COFs can be constructed from a single foundational blueprint by substituting monomers and linkages with similar geometries. [23]

This self-assembly leads to the formation of 3D COF structures, where stacked layers create channels that run through the material. By carefully selecting monomers and defining how they connect, it becomes possible to control both the molecular-scale features and the overall architecture of COFs, optimizing them for specific applications.[24]

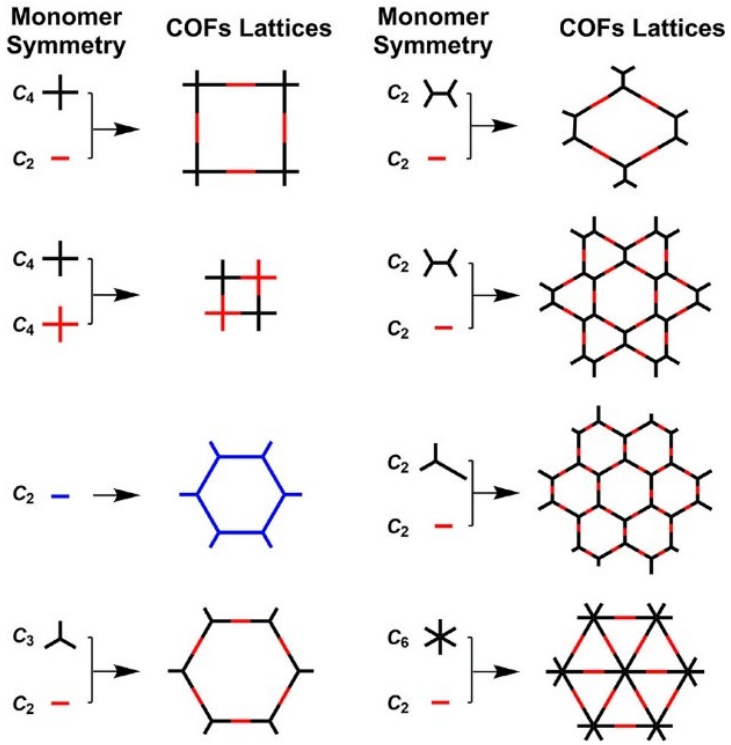

Figure 2: Basic topological diagrams of 2D COFs [25]

2.1.2. 2D and 3D Structure

The architecture of 2D COFs offers exceptional design flexibility, allowing the prediction of pore sizes and shapes through careful selection of building units and bonding patterns. Topology diagrams as shown in Figure 2 serve as blueprints for these structures. Common pore geometries including hexagons [1], triangles [26], tetragons [27], kagome [28] and rhomboids [29] lattices, can be created by combining monomers with specific symmetries. Diverse pore configurations can be achieved by varying monomer arrangements and synthesis strategies. [30] In contrast, the range of 3D COFs remains limited due to the difficulty of forming highly crystalline structures and the scarcity of suitable 3D building blocks. The design versatility of 2D COFs arises from their foundational topology, comprising both regular (isotropic) [31] and irregular (anisotropic) [32] polygonal frameworks with discrete pores and intricate lattice arrangements. This topological richness enables structural variations, with specific architectures, resulting from different combinations of linkers and monomers within a given topological framework. [25]

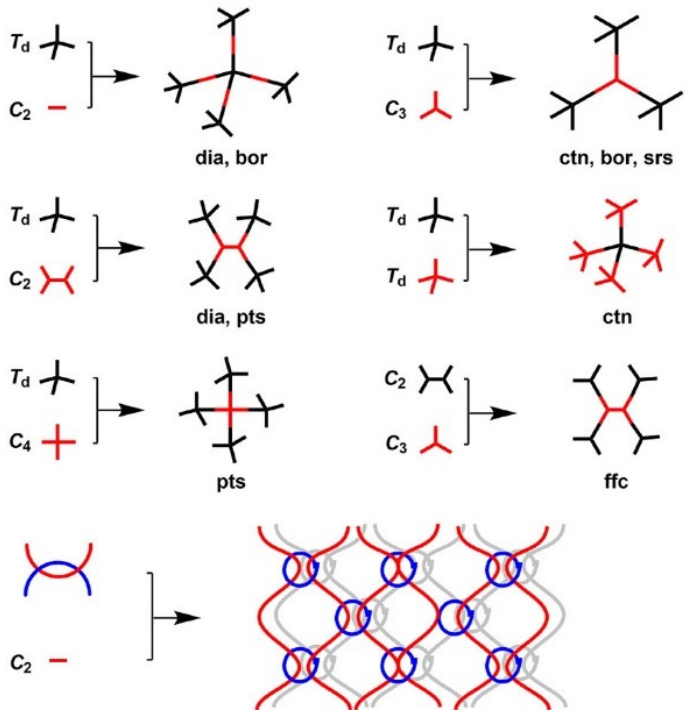

Figure 3: Linkage with T_d geometries [25]

The design of 3D COFs requires at least one building block with T_d or orthogonal geometry, unlike 2D COFs, which typically rely on planar building blocks. This non-planar geometry directs the polymer backbone to extend into a fully covalently bonded

three-dimensional framework. Figure 3 shows the resulting 3D COF structure, composed of interpenetrated and folded polymer chains, forms pores based on combinations of T_d or orthogonal nodes with symmetries such as C1, C2, C3, C4, and T_d. [33] The limited availability of suitable 3D building blocks and the complexity of achieving well-ordered crystalline structures make 3D COFs significantly rarer than 2D COFs. The integration of T_d or orthogonal geometries, often linked to additional nodes with C2, C3, or C4 symmetries, provides the structural precision needed for constructing robust, three-dimensional networks. This approach expands the design possibilities but remains a challenging area of COFs synthesis. [25]

2.1.3. Linkage

Strong covalent bonds typically lead to amorphous or poorly crystalline polymers. [34] To produce highly crystalline COF materials, reversible chemical bonding and a reaction rate within a specific range are essential. This allows the monomers to correct any flaws in the framework autonomously. [35] As a result, dynamic covalent chemistry (DCC) is commonly employed to synthesis crystalline COFs. [13] Interestingly, there have also been instances where COFs have been constructed using processes traditionally considered irreversible. [30] Due to the nature of the covalent linkages, COFs can now be categorized into various types, including boroxin/boronate ester, imine, azine, imide, triazine, hydrazone, C=C, 1,4-dioxine, and others. These diverse chemical linkages enable the creation of a wide range of COF structures with distinct properties. [30]

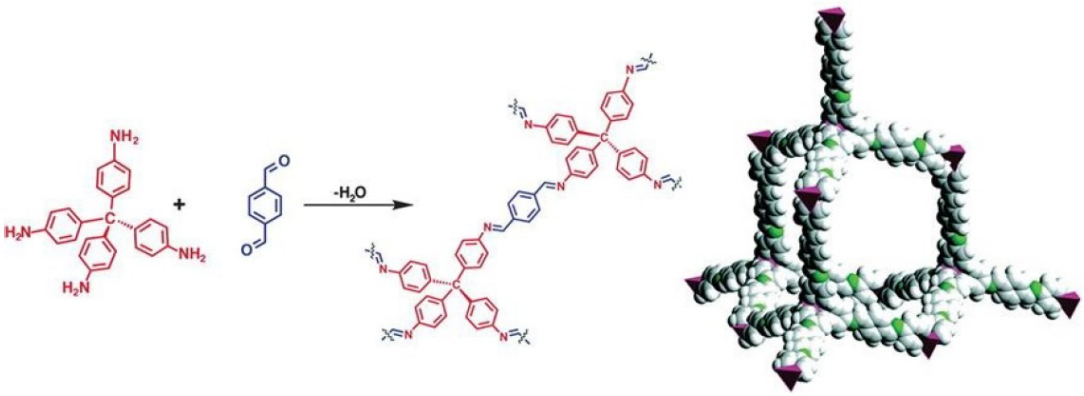

Figure 4: COF-300, imine linked [30]

In this work, COFs with imine linkage were examined. An imine bond is formed when an aromatic amine reacts with an aldehyde in the presence of a Lewis acid catalyst. COFs that use imine linkages have a higher chemical stability but are usually less crystalline than COFs with boroxine or boronate ester bonds. The increased stability allows these COFs to maintain their structural integrity under many conditions, including exposure to organic solvents, water, acids, and bases. [30] In 2009, the first imine-linked COF, COF-300, was synthesized by dehydrating tetra-(4-anilyl)methane, which has a tetrahedral shape, with terephthalaldehyde, a linear compound. [36] Imines have become a popular choice for COF synthesis due to their diverse selection of monomers, the remarkable stability of the resulting frameworks, and the ability of nitrogen atoms to engage in coordination or chemical reactions, providing further opportunities for functionalization. [30]

2.1.4. Synthesis

A range of synthesis methods for COFs has recently been developed, including solution synthesis, solvothermal synthesis, ionothermal synthesis, microwave-assisted synthesis, and mechanochemical synthesis. [30]

The synthesis of COFs generally demands severe experimental conditions, such as reactions in a sealed Pyrex tube, an inert atmosphere, and prolonged reaction durations. The solution synthesis is simply achieved by stirring the solution at room temperature, for a moderate time. [37]

Solvothermal synthesis is the most widely used method for preparing COFs. These frameworks are synthesized through chemical reactions of organic monomers in sealed systems under appropriate solvents, temperatures, and autogenic pressures. Typically, the process begins by mixing monomers with solvents, adding them to a Pyrex tube, and dispersing the mixture via sonication. Oxygen is removed from the system using a liquid nitrogen thawing cycle repeated three times. The Pyrex tube is then sealed with a flamethrower and placed in a thermostatic oven for a specified period. Once the system cools to room temperature, the resulting insoluble materials are collected through centrifugation. [30]

Ionothermal synthesis involves using ionic liquids as both the solvent and a potential template or structure-directing agent in solid formation. This method closely parallels hydrothermal synthesis, in which water serves as the solvent. [38] This innovative approach eliminates the need for large quantities of environmentally harmful solvents and catalysts while significantly reducing reaction time compared to traditional solvothermal methods. [9,38,39]

The mechanochemical synthesis of COFs was initially optimized on a small scale using a mortar and pestle. The resulting material is thoroughly mixed with water until it reaches a dough-like consistency, then transferred to a glass vial for further heating. After purification, the material is dried in an oven. For bulk-scale synthesis, COFs can be produced using a planetary mixer. [18]

Microwave-assisted synthesis begins by dissolving the desired precursors in an appropriate solvent or solvent mixture. This solution is then transferred to a sealed microwave-compatible reaction vessel under an inert. The reaction mixture is heated using microwave irradiation at a controlled temperature and power setting while stirring. [19]

The choice of method depends on factors such as the solubility and stability of the monomers, as well as the reactivity and reversibility of the reaction systems. In addition to selecting the appropriate synthesis technique, experimental parameters like temperature, reaction time, and solvent play a crucial role for the outcome of the synthesis. One of the key challenges in COF production is achieving improved crystallinity, which has led to the development of several techniques aimed at enhancing this property. Despite these advancements, large-scale production of COFs with high crystallinity remains difficult, and further optimization is needed for rapid and efficient synthesis. [24,30]

There were already efforts in setting up a continuous flow approach for the synthesis, [17,40,41] by using a very simple reactor design usually only consisting of a tube and a simple T - connector as a mixer. [17,40] Others heated there coiled reactor, to reduce the residence time to range of 5 seconds to 6 minutes and achieving a continuous production of 45 minutes. [41]

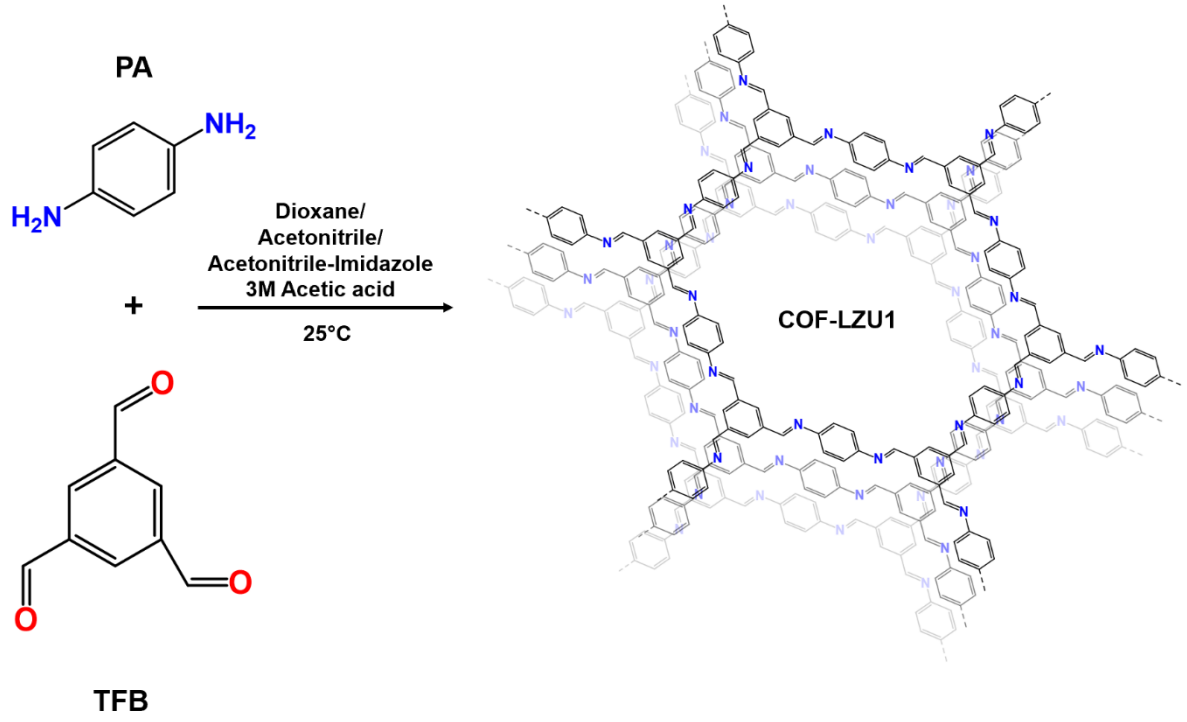

Figure 5: Chemical equation of the reaction performed for the thesis [42]

Herin, the solution suspension synthesis is used to synthesize the two-dimensional imine-linked COF-LZU1 [17]. This COF was chosen since the price of the educts is moderate and there are several literature references to start with. Furthermore, is the reaction procedure rather simple compared to others like mentioned before. [43] As

the starting materials 1,3,5-triformylbenzene (TFB) as a linker and p-phenylenediamine (PDA) as a linkage form the 3D framework of COF-LZU1 (see Figure 3). Acetic acid was applied as catalyst for the reaction and the formation of solids. The process was executed at room temperature and with dioxane, [17] acetonitrile and acetonitrile with 20 mg mL^{-1} imidazole as solvent. The corresponding chemical equation is illustrated in Figure 5.

2.2. Kinetics of Homogeneous Reactions

The study of reaction kinetics is fundamental in chemical engineering, as it provides insights into the reaction rate and mechanisms of chemical reactions. A key aspect of kinetics is the reaction rate, which describes how quickly reactants are converted. Several factors, including reactant concentrations, temperature and the presence of catalysts, affect this rate. The relationship between these factors is mathematically expressed through the reaction rate equation: [44]

$$-r_A = k \cdot c_A^n \qquad \textit{Equation 1}$$

where r_A is the reaction rate, k is the reaction rate constant, c_A represents the concentration of reactant A, and n denotes the reaction order for compound A.

The reaction rate constant k is a fundamental parameter that determines the speed of a reaction under given conditions. Unlike concentration, which changes throughout a reaction, the rate constant remains fixed for a specific reaction at a constant temperature. However, it exhibits strong temperature dependence, which is described by the Arrhenius equation: [44]

$$k = A \cdot e^{-\frac{E_A}{R \cdot T}} \qquad \textit{Equation 2}$$

where A is the pre-exponential factor, E_A is the activation energy, R is the universal gas constant, and T is the absolute temperature. As temperature increases, the reaction rate typically rises due to higher molecular kinetic energy, which enhances the probability of successful collisions between reactant molecules. This relationship is crucial in reactor design, as controlling the temperature allows optimisation of reaction rates in industrial processes. [44]

The reaction order, n, indicates how the rate of reaction depends on the concentration of reactants. It is an experimentally determined parameter and can take integer or fractional values. The most common reaction orders include: Zero-order reactions ($n = 0$): The reaction rate is independent of the concentration of reactants, meaning the reaction proceeds at a constant rate until the reactants are depleted. This is often observed in catalyzed reactions where the surface of a catalyst is saturated. First-order reactions ($n = 1$): The rate is directly proportional to the concentration of a single reactant. A classic example is radioactive decay or simple unimolecular decomposition reactions. Second-order reactions ($n = 2$): The rate depends on either the square of

the concentration of a single reactant or the product of two reactant concentrations each with first order. These reactions are common in biomolecular processes and SN_2 reactions. [44]

The determination of reaction order is essential for understanding reaction mechanisms and predicting concentration changes over time. Several methods exist for determining reaction order and the corresponding rate constant. The method of initial rates involves measuring the reaction rate at different initial reactant concentrations and analysing how the rate changes. Another approach is the integral method, where experimental concentration data are fitted to theoretical rate laws to identify the best match. Additionally, the differential method uses logarithmic transformations to graphically analyse reaction rate trends. [44]

In the approach for this thesis, the reaction order and rate constant were determined by fitting experimental results of the peak intensity of the collected Raman spectra versus time to models representing zero-order, first-order, and second-order reactions. It was assumed that the rate limiting reactant was TFB and PDA is in high excess. Thus, the reaction kinetics can be determined by monitoring the conversion of TFB. Nonlinear regression was used to fit each model to the data, employing least-squares minimization to find the best-fitting parameters for each reaction order. For each model, the sum of squared errors (SSE) was calculated to evaluate the discrepancy between the measured and fitted values. Additionally, the coefficient of determination (R^2) was computed to assess the goodness of fit, with higher R^2 values indicating better model accuracy. The model with the highest R^2 value was identified as the best fit, and the corresponding reaction order and rate constant were extracted. This method allows for a systematic comparison of different reaction orders, ensuring the most appropriate kinetic model is selected based on the residuals and the goodness of fit.

2.3. Gas Adsorption and the BET Theory

One popular technique for describing the surface characteristics of materials, especially ceramics, is the adsorption of gases onto porous solids. It is possible to deduce or quantify important material properties by examining surface parameters. The link between an adsorbed gas's volume and relative pressure is the foundation for this investigation. [45] In 1938, Stephen Brunauer, Paul Emmett, and Edward Teller developed the Brunauer–Emmett–Teller (BET) theory, which expands Langmuir's adsorption model to multilayer adsorption systems. The BET theory assumes that adsorbed molecules in multilayers maintain dynamic equilibrium with the vapor phase to determine the specific surface area. [46]

This method typically employs probing gases (adsorbates) that do not chemically react with the material surface. The most used adsorbate in BET analysis is nitrogen, typically measured at its boiling temperature (77 K). [47] Other gases, including argon, carbon dioxide, and water vapor, are also used to study surface area variations under different conditions. [48]

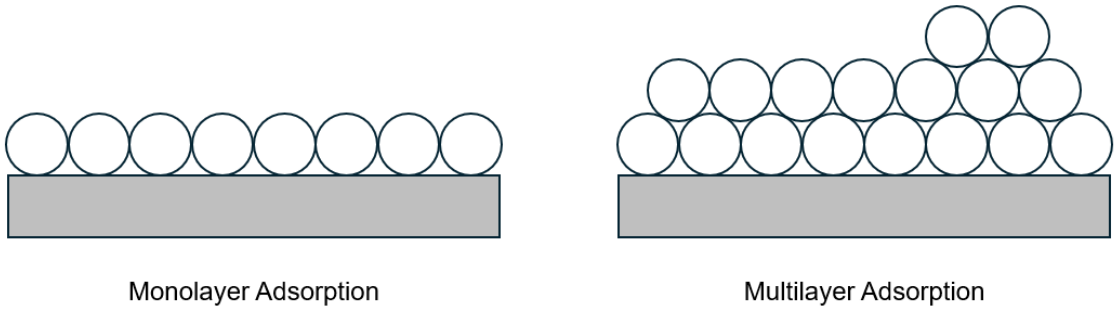

Figure 6: Monolayer adsorption and multilayer adsorption of N_2 molecules on a surface

During physical adsorption, at very low relative pressures, the most energetic adsorption sites, typically located within narrow pores where overlapping potentials exist, are the first to be occupied. Other high-energy sites include surface steps where adsorbate molecules can interact with multiple planes of surface atoms. In materials containing heteroatoms, such as organic solids or impure substances, variations in adsorption potential arise due to the chemical nature of exposed functional groups. While higher-energy sites retain adsorbed molecules longer, adsorption still occurs on lower-energy sites as pressure increases. As a result, progressive surface coverage leads to the adsorption of additional molecular layers before a complete monolayer is formed. [45]

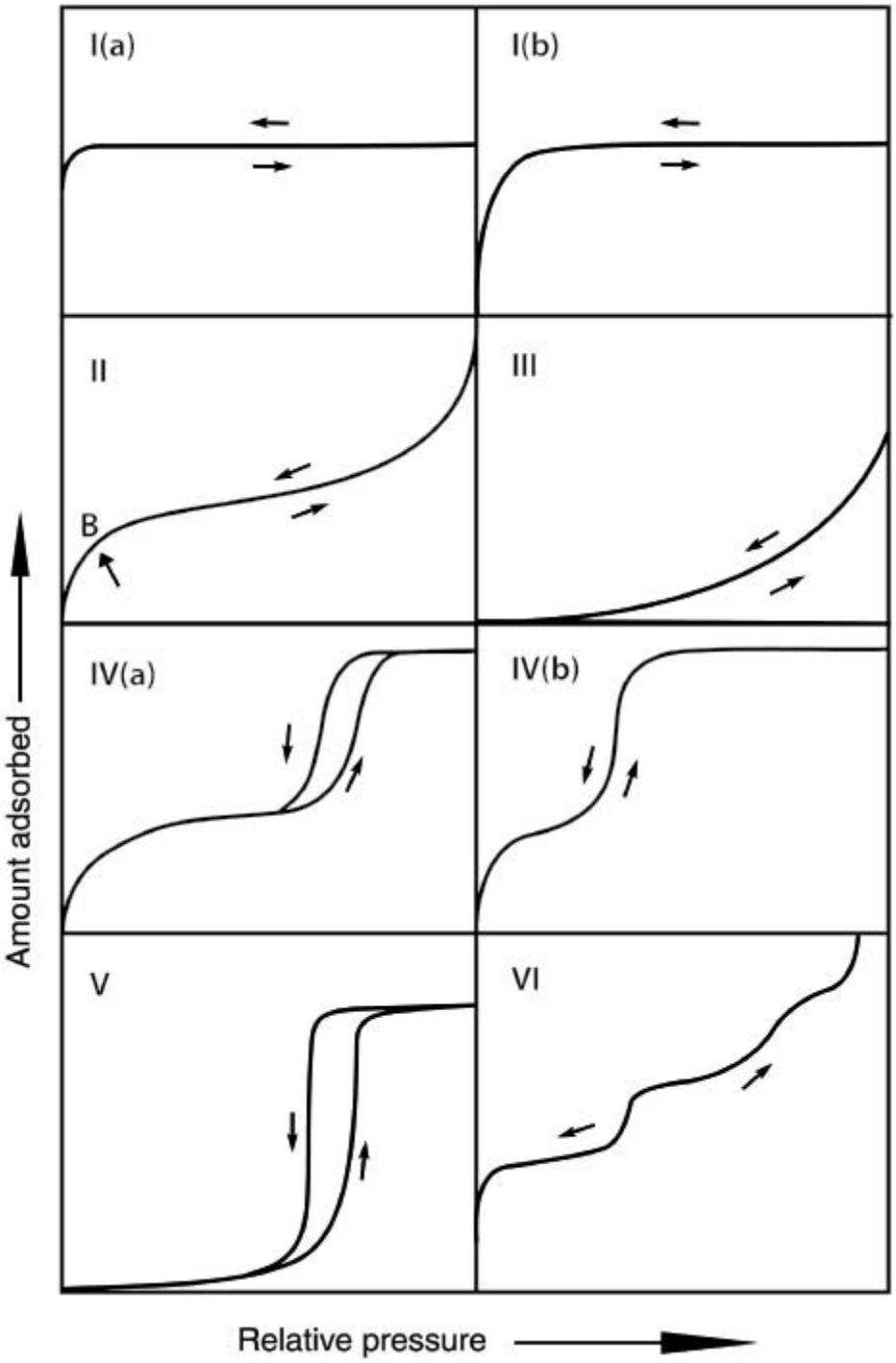

Figure 7: Adsorption isotherms classification [47]

The BET theory provides a practical means of determining the number of molecules required to form a monolayer, even though an ideal monolayer is never truly achieved. The collected adsorption data is typically represented as a BET isotherm, which illustrates the relationship between the amount of gas adsorbed and the relative pressure. Since the specific surface area is a scale-dependent property with no

absolute value, BET-derived measurements vary depending on the choice of adsorbate and its molecular adsorption cross-section. [45]

By extending Langmuir's 1916 theory [49], the BET model was the first to offer a theoretical framework for understanding the transition from monolayer completion to multilayer growth. [50] This advancement has made BET analysis a fundamental tool for studying surface characteristics, particularly in porous and high-surface-area materials. [45]

2.4. Fourier Transform Infrared (FTIR) Spectroscopy

Fourier transform infrared (FTIR) spectroscopy is a non-destructive characterization and efficient method for investigating the surface properties of a material. [48] It uses the vibrational modes of molecules to create a molecular fingerprint. FTIR can be used to identify reactive surface sites, analyse chemical bonds and determine the chemical composition. In addition to detecting chemical reactions, identifying isomers, and evaluating sample purity, this technique is frequently employed in qualitative and structural analysis. [48]

FTIR spectroscopy operates by measuring the infrared spectra of substances through an interferogram, which is then transformed into a spectral output using Fourier transformation. An optical detection unit and a computer for data processing typically make up the system. [51] Efficiency is one of FTIR's main benefits; it involves little sample preparation, permits the examination of both liquids and solids, and only requires modest sample volumes (microliters for liquids and micrograms for solids). Furthermore, because of its high signal-to-noise ratio, reliable energy throughput, remarkable precision, and stability, FTIR is a widely used and affordable analytical technique. [48]

An interferometer, an optical instrument that creates the interferogram, is the central component of any FTIR system. One beam of light is split into two by the interferometer, and these beams follow different pathways before being recombined. The optical path difference (δ) is the difference between these route lengths. Zero path difference (ZPD) occurs when δ = 0 and the pathways have the same length. [51]

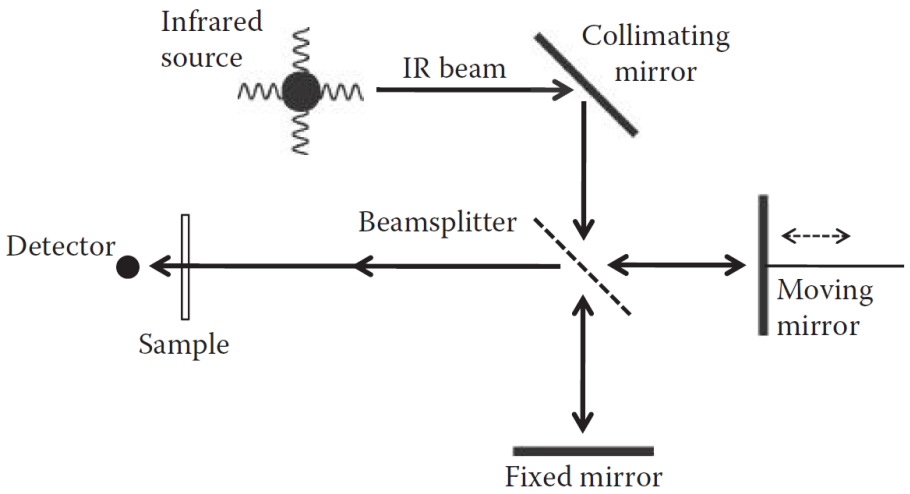

Figure 8: Michelson interferometer [51]

The interferometer consists of four primary components: [51]

- Infrared Source and Collimating Mirror – Directs parallel rays of infrared light into the system.
- Fixed Mirror – A stationary mirror that reflects part of the incoming light.
- Moving Mirror – Capable of shifting position, altering the optical path difference.
- Beamsplitter – A key optical component that partially transmits and partially reflects incoming light, directing beams toward both mirrors.

The components are shown in Figure 8. As the moving mirror shifts, the two reflected beams recombine at the beamsplitter, creating an interference pattern that contains spectral information about the sample. This combined light then passes through the sample before reaching the detector, where the Fourier transform is applied to extract the absorption spectrum. [51]

FTIR spectroscopy has revolutionized surface characterization by providing rapid, accurate, and non-destructive chemical analysis. Its application extends across numerous scientific and industrial fields, including materials science, pharmaceuticals, and environmental studies, making it an indispensable analytical tool. [48]

2.5. Small-angle X-ray scattering (SAXS)

An important technique for describing the structure and order of nanostructured materials, biomolecules, fluids, and suspensions is small-angle X-ray scattering or SAXS. [52] The fact that SAXS measurements can be carried out with laboratory-based equipment is one of its main benefits, as it opens up a wide range of applications. [53]

When waves, like X-rays, hit an obstruction and disperse, diffraction occurs. Every electron in the substance is a source of a new and scattered wave. The phases of these scattered waves are connected because they stay coherent and have the same wavelength as the incident X-rays. A pattern of diffraction is created when these waves interfere with each other. [54]

Diffraction interference can be either beneficial or detrimental. When waves are in phase, they reinforce one another and increase the intensity of the scattered waves, a phenomenon known as constructive interference. On the other hand, destructive interference results in cancellation and diminished intensity. This happens when waves are out of phase. The constructive and destructive interferences are combined to generate the diffraction pattern. [54]

Reciprocity is the inverse relationship between the size of the scattering item and the angle at which scattering is seen. While smaller objects scatter at bigger angles, larger objects scatter stronger at smaller angles. In SAXS, where small-angle scattering provides information about large-scale structures, this idea is very important. [54]

According to the reciprocity principle, SAXS is particularly sensitive to larger structural features within a sample, typically ranging from around 10 Å to several thousand Å. This makes it ideal for studying macromolecules in solution, voids in materials, and other electron density inhomogeneities. [54]

SAXS is based on electron density contrast since X-rays scatter from electrons. The difference in electron density between the scattering objects and their surrounding medium determines the strength of SAXS signals. At all angles other than zero, the scattered waves cancel out if the electron density is constant across the sample. As a result, SAXS can only identify areas with notable variations in electron density. A crucial component of SAXS measurements is this contrast-based detection. [54]

The Guinier approximation is one of the most crucial analytical techniques in SAXS since it offers a way to calculate the total size of a scattering object. A Gaussian function is approximate the scattering curve at very small angles for objects that are

not too big or anisotropic. The radius of gyration (Rg) of the scattering object can be found by examining the slope of a Guinier plot, which is a plot of the logarithm of scattered intensity versus the square of the scattering angle. Similar to the radius of inertia in physics, Rg is a measurement of an object's total dimensions. It is crucial to remember that the Guinier approximation is only accurate for a relatively small range of angles. [53]

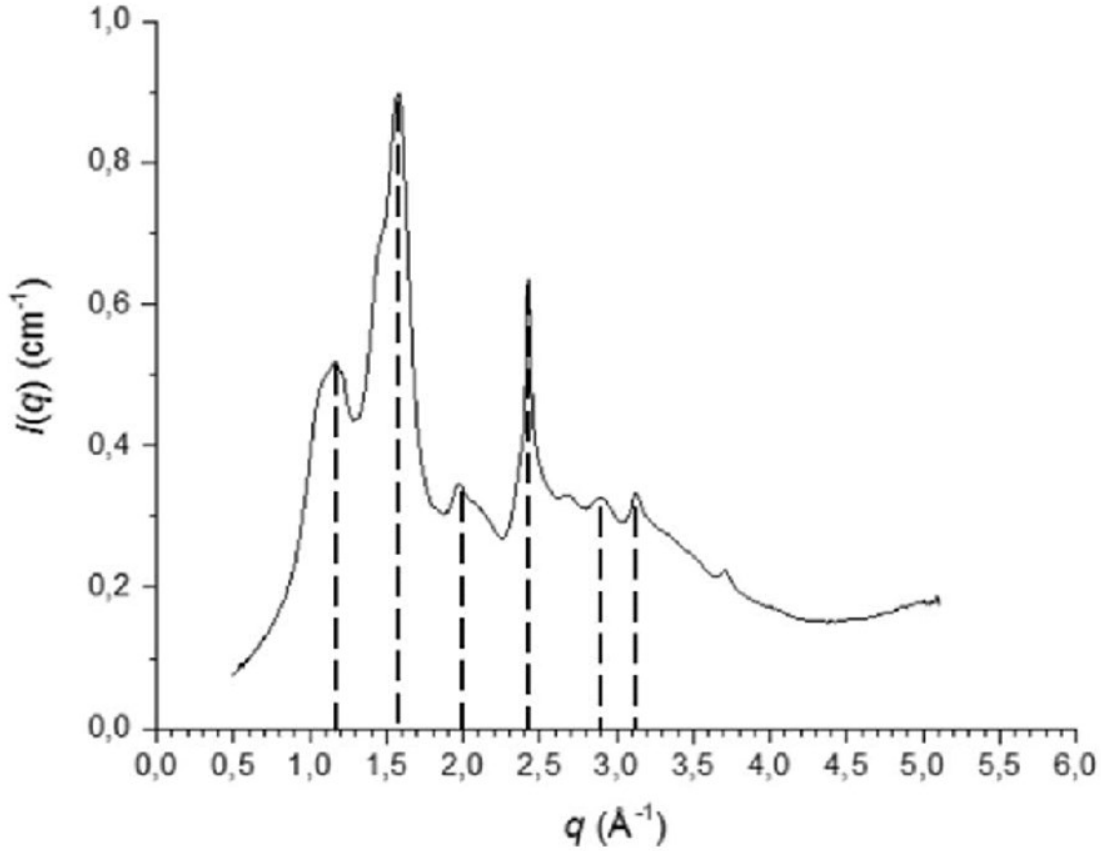

Figure 9: Typical result of a SAXS measurement (cellulose fiber) [55]

3. Raman Spectroscopy

Raman spectroscopy is a powerful analytical technique used to study vibrational, rotational, and other low-frequency modes in a system. It relies on the inelastic scattering of monochromatic light, usually from a laser in the visible, near-infrared, or near-ultraviolet range. When light interacts with a molecule, most photons are elastically scattered (Rayleigh scattering) with no change in energy. However, a small fraction of photons undergoes inelastic scattering, where energy is either gained or lost by the molecule. This energy shift corresponds to vibrational energy levels within the molecule, providing a unique fingerprint for molecular identification and structural characterization. [56]

A molecule can be viewed as a system of interconnected atoms held together by chemical bonds, which can be modeled as springs. The atoms vibrate around their equilibrium positions, and these vibrations are quantified, i.e., they can occur only at discrete energy levels. [57]

These vibrations can be described as a combination of normal modes, each with its own characteristic frequency. Certain groups of atoms within a molecule, like a CH_2 group or a carbonyl group, give rise to characteristic vibrations within specific frequency ranges, often referred to as group frequencies. [57]

These frequencies, summarized in correlation tables are invaluable for interpreting Raman spectra and identifying functional groups in complex molecules. [56]

Sample preparation is minimal in Raman spectroscopy, as samples can be analyzed in various states (solid, liquid, gas) and often directly in their containers. However, sample fluorescence can sometimes be a major interference, and strategies to minimize this include optimizing laser wavelength, sample dilution, or using time-resolved techniques. [58]

A typical Raman spectrometer consists of a laser source, sample illumination and collection optics, a wavelength selector (usually a monochromator or an interferometer), and a detector (such as a photomultiplier tube or a charge-coupled device). [57] The entire layout of the Raman spectrometer is shown in Figure 10.

The choice of laser wavelength and detector depends on the specific application. Visible excitation is commonly used, but near-infrared excitation coupled with Fourier-transform interferometry (FT-Raman) offers advantages in reducing fluorescence. [58]

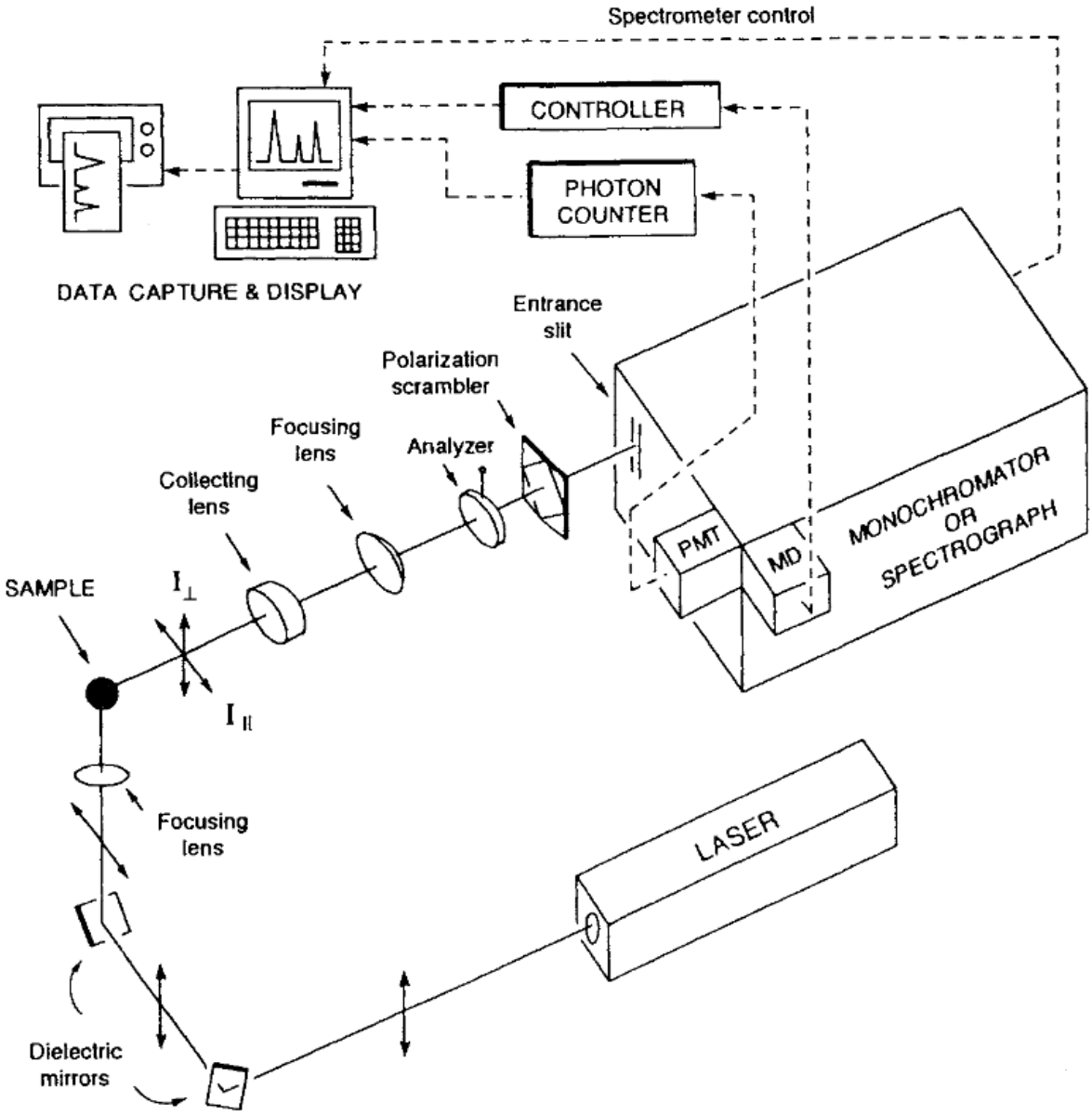

Figure 10: Schematic illustration of the main components of a Raman Spectroscope [57]

4. Materials and Methods

4.1. Material

The linker 1,3,5-triformylbenzene (>98%) (TFB) was purchased from TCI, while the linkage p-phenylenediamine (≥98%) (PDA) was acquired from Roth. Dioxane (≥99.5%, stabilized) and Acetonitrile (≥99.9%) were used as the reaction solvent, provided by Roth. Imidazole (≥99.9%) was bought from Sigma-Aldrich. The catalyst, Acetic Acid, is from Honeywell Fluka (≥99.8%). All chemicals were used without further treatments. The batch synthesis was carried out in 20 mL glass vials with rolled rims.

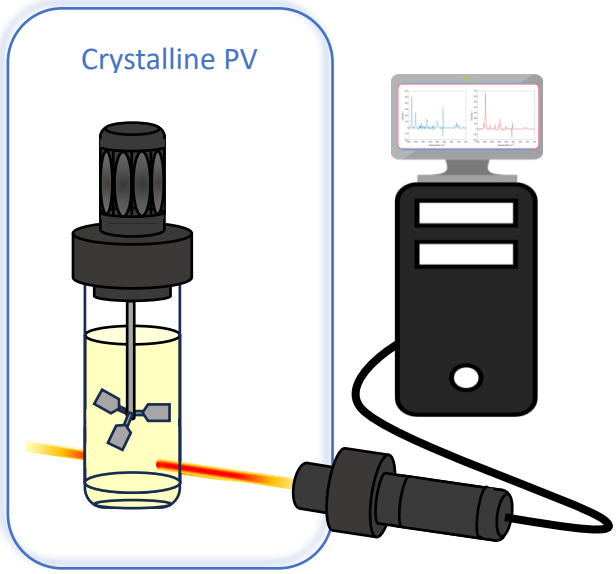

Figure 11: Schematics of the Raman experiment with stirred glass vial and computer connection [42]

The Raman experiments were done in the Technobis Crystalline® system [59] to ensure accurate and constant process parameters. As a reactor special 8 mL glass vials were used, to minimize the influence of the glass vial on the measurement. The experimental setup is schematically illustrated in Figure 11. The Crystalline allows stirring of the reaction solution with a three-bladed impeller for sufficient mixing during the reaction without interfering with the laser beam of the Raman probe. We used the Kaiser Raman RXN2 [60] with the MultiRxn Probe - 785nm for all the experiments and the provided software for the manufacturer.

The continuous flow setup was realised with two VIT-FIT Lambda [61] syringe pumps and stainless-steel syringes for the reactants, in some experiments a Langraf LA - 120 [62] was used. The streams were merged with a PTFE T - connector from Upchurch Scientific and then intensively mixed during the reaction in a PTFE tube with an inner

diameter of 0.8 mm, which submerged in an ultrasonic bath. To provide the necessary reaction time, the length was adjusted to 2850 mm resulting in a hydraulic resistance time of 10 min with a flow rate of 50 µL min^{-1} of each educt stream.

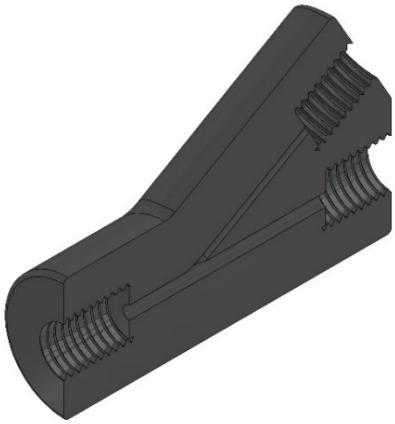

Figure 12: Sectional view of the Y-connector

The catalyst acetic acid was continuously added with a SyrDos syringe pump from HiTEC ZANG [63] with glass syringes at the self-designed and 3D-printed Y - connector. The inner diameter for the main stream was 1.6 mm and the diameter for the catalyst stream was 0.8 mm. The total length of the connector was 40 mm, with the two lines positioned at an angle of 30° to each other. The connector is depicted in Figure 12 and was designed to avoid clogging inside the small channels when the acid encounters the reaction solution. It was printed with the Phrozen Sonic Mini 8K S [64] masked stereolithography 3D resin printer. The resin for the printer was Phrozen Aqua 3D Printing Resin Oat White [65] and TR250LV High Temp 3D Printing Resin Gray [66].

Solids are formed right after the first contact with the catalyst. Therefore, the second part of the tubular reactor has a bigger inner diameter of 1.6 mm to reduce the probability of clogging. The basic length of this section is 3000 mm, it was altered individually to meet the necessary residence time if the flow rate was changed for an experiment.

Figure 13: Sectional view of the three input Y-connector

For the slug flow setup with N_2 the Y - connector was redesigned to mix three inputs, with the same dimensions as before. As shown in Figure 13 the input for the N_2 stream was ahead of the input where the acetic acid was added, to form the slugs before the solids were formed.

For downstream processing, solvents including methanol, acetone, dichloromethane, and hexane were also supplied by Roth.

At the end of the setup, the output stream flows into a paper filter from Karl Hecht, folded DIN 5313722s with a thickness of 0.16 mm, that is placed in a funnel to separate the COF product from the liquid stream. A stream of methanol is pumped with a peristaltic pump into the funnel to wash the solids continuously and quench the reaction.

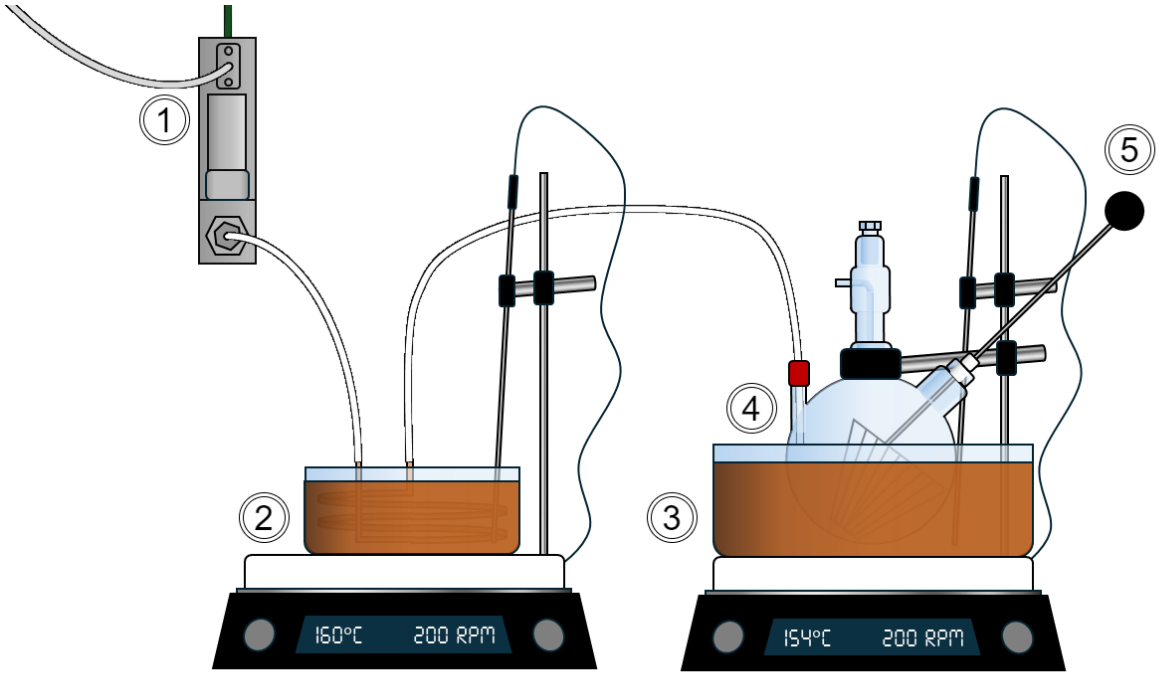

Figure 14: Drying setup with (1) mass flow controller for the N_2 stream; (2) temperature-controlled oil bath on a stirred heating plate with the copper coil as heat transfer element; (3) temperature-controlled oil bath on a stirred heating plate for the product flask; (4) three-neck flask containing the filter with the product; (5) thermometer to control the drying temperature

The obtained product was dried in a three-necked flask at 120°C under a nitrogen atmosphere. The nitrogen was preheated using a heat exchanger designed with a copper coil in an oil bath. The N_2 flowrate was regulated with a mass flow controller form Bronkhorst. The three-necked flask was similarly heated in an oil bath to maintain the desired temperature. Both oil baths were controlled using IKA C-MAG HS7 thermostats. The experimental setup is shown in Figure 14, with a thermometer placed near the product in the filter to monitor the temperature of the surrounding nitrogen atmosphere. [67]

4.2. Methods

4.2.1. Batch Reaction of the Covalent Organic Frameworks

For the initial batch reactions, a series of experiments was conducted to assess the impact of reaction time and work-up procedures. In these experiments, 480 mg of 1,3,5-triformylbenzene (TFB) was dissolved in 30 mL of dioxane, and 480 mg of p-phenylenediamine (PDA) was dissolved in 30 mL of dioxane using an ultrasonic bath. Initially, 5 mL of the TFB solution and 5 mL of the PDA solution were pipetted into six separate glass vials and homogenized for 10 minutes in the ultrasonic bath. Following this, 2 mL of 3 M acetic acid in water was added to each vial and gently swirled to mix thoroughly. The vials were sealed and left at room temperature for varying reaction times. V1, V2, G1, and G2 had a reaction time of three days, while V3 and G3 had a reaction time of three hours. These first experiments were performed during my construction theses.

The downstream processing differed depending on the sample. For V1, V2, and V3, the solid product was separated from the reaction mixture by filtration and washed with acetone. Next, the solids were washed with dichloromethane and subsequently three times washes with methanol. This washing and filtration process was performed using filter paper and a filter frit, aided by a water jet vacuum pump. The product from V2 underwent sonication in methanol for two 10-minute cycles, but this caused the solids' structure to break down and significantly reduced the volume. After final filtration, the yellow COF product was placed in a desiccator for one day and then in a drying cabinet for another day at 60°C.

The samples G1, G2, and G3 were quenched with methanol. First, 3 mL of methanol was slowly added twice to each vial, followed by decanting. Afterward, 2.5 mL of methanol was added to the bottom of the vial. This process was repeated twice to almost clear the reaction solution. Afterwards, the solids were filtered via filter paper and a funnel and washed with 150 mL of methanol. The product was transferred to glass vials containing dichloromethane, and every hour, the dichloromethane in the vials for samples G1 and G3 was replaced with fresh dichloromethane for three hours. The solvent in G2 was refreshed after 10 minutes in an ultrasonic bath for three cycles. Following this, the dichloromethane was replaced by hexane. For sample G1, hexane was renewed twice every 10 minutes, while for G2, it was renewed three times every 10 minutes, and for G3, once after 10 minutes. The residence time in hexane also

varied among the samples: G1 and G2 were kept in hexane for 40 hours and 43 hours, respectively, while G3 remained in the solvent for 68 hours.

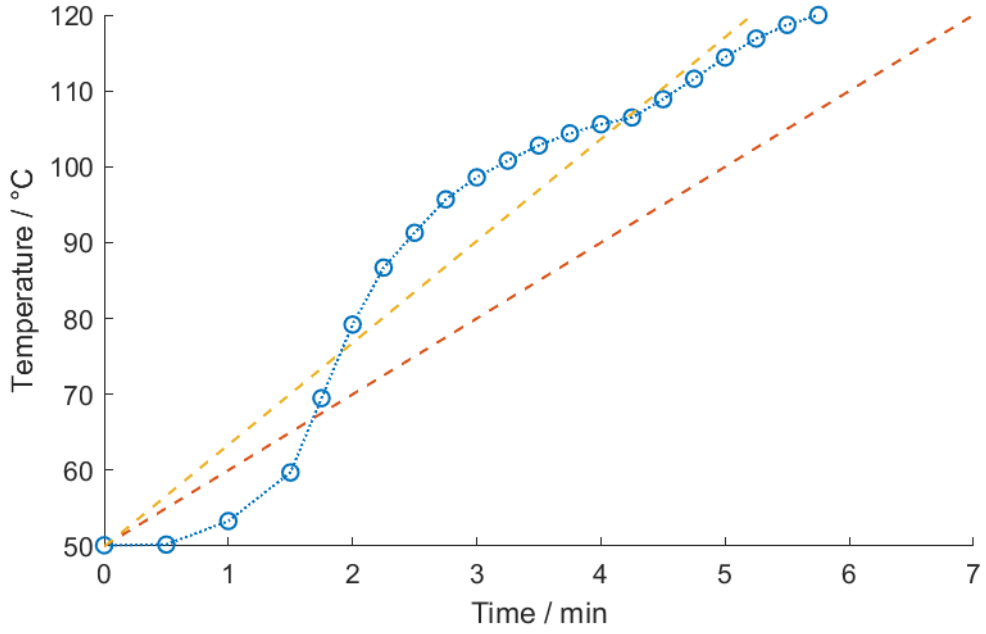

Figure 15: Temperature over time, Linear fit of the temperature over time, Target temperature ramp

Finally, all samples were filtered using filter paper and dried under a nitrogen atmosphere at 120°C for three hours once the desired temperature was reached. The temperature ramp was aimed to be 10°C per minute, but the actual ramp achieved with the setup was 13.5°C per minute. [67] **Fehler! Verweisquelle konnte nicht gefunden werden.** shows the measured temperature rise over time, comparing the actual ramp with the desired temperature increase.

Table 1: Comparison of the reaction time and downstream processing of each sample

Sample	V1	V2	V3	G1	G2	G3
Reaction Time	3 days	3 days	3 h	3 days	3 days	3 h
Filtration	Water jet pump	Water jet pump	Water jet pump	Gravity	Gravity	Gravity
1. Solvent	Acetone	Acetone	Acetone	Methanol	Methanol	Methanol
2. Solvent	DCM Wash	DCM 2x 10 min Sonicated	DCM Wash	DCM 3x 1 h Resting	DCM 3x 10 min Sonicated	DCM 3x 1 h Resting
3. Solvent	Methanol Wash	Methanol Wash	Methanol Wash	n-Hexane Resting	n-Hexane Resting	n-Hexane Resting
Drying	Vacuum 1 day Air 60°C 1 day	Vacuum 1 day Air 60°C 1 day	Vacuum 1 day Air 60°C 1 day	N_2 120°C 3 h	N_2 120°C 3 h	N_2 120°C 3 h

A summary of the different downstream processing methods and reaction times is provided in **Fehler! Verweisquelle konnte nicht gefunden werden.**.

The different samples were analysed using Brunauer–Emmett–Teller (BET) measurements to determine their surface area. To assess the crystallinity, both small-angle X-ray scattering (SAXS) and wide-angle X-ray scattering (WAXS) measurements were performed. For a more detailed understanding of the structure and surface morphology, the products were examined with a scanning electron microscope (SEM) and an optical microscope. In addition, the samples were characterized using Fourier-transform infrared spectroscopy (FTIR) to gather further insights into their chemical composition and functional groups.

Since there were also continuous flow experiments carried out with slug flow, it was necessary to test the existing reaction parameters with water and later acetonitrile as solvent. Furthermore, it was also tested to see if imidazole has an influence on the product.

Therefore, a batch reaction was prepared by adding 64.8 mg of TFB, 66 mg of PDA, and 200 mg of imidazole to 10 mL of water. It was stirred for an initial 5 min, but since it wasn`t dissolved properly it was stirred for another 25 min.
In the next step, 50 ml of methanol was dripped into the reaction flask and left for three hours before it was worked up with the same procedure as the G series.
As there were still solids left after 30 minutes of stirring, solubility tests with a water imidazole solution with a concentration of 20 mg mL^{-1} were conducted. TFB and PDA were individually added to the water imidazole solution and diluted until all solids were dissolved.
Expecting better results, this procedure was repeated with acetonitrile and later first batch reactions were performed before examining the reaction with the Raman device. For the batch reaction, 35 mg of TFB and 35 mg of PDA were dissolved in 3.5 mL pure acetonitrile and 3.5 mL acetonitrile imidazole solution with a concentration of 20 mg mL^{-1} using an ultrasonic bath. Following this, 3 ml of each solution was put into two 20 mL glass vials with rolled rims. One for the solution with imidazole and one for the solution without. Both vials were sonicated for 10 min to mix the reactants and allowed to stand for 3 hours to promote the formation of solids. Afterwards, the same postprocessing procedure was applied to the product.
To investigate the influence of oxygen on the reaction and its impact on the product, since oxidation is detrimental to the formation of COFs, the final batch experiments were conducted using dioxane, with the reaction solution being flushed with nitrogen during the process.
The G3 procedure was repeated, one vial with N_2 flushing and one without as in the first experiments. The mass flow controller was set to a minimum where approximately five bubbles per second were formed. An exact flow rate cannot be provided, since the mass flow controller was in a range that was very unstable and had to be readjusted several times to keep the same flow rate. The nitrogen stream was introduced after the reactants were sonicated and the acetic acid was added.

4.2.2. Raman Experiments

The Raman analysis was used for a variety of experiments. First, the characteristic peaks of each component were investigated. Therefore, the solvent dioxane was filled into the glass vial and measured to receive a reference spectrum. Afterwards, the linker TFB and the linkage PDA were measured individually. The reference spectra were determined in triplicate to minimize errors. The scan time was determined with the software and then set to 10 seconds. The range of the measured spectrum reached from a wavenumber of 200 cm^{-1} to 1800 cm^{-1}.

To carry out the reactions, dioxane was first added to the vial to obtain a reference spectrum for the solvent. Next, the first reactant, TFB, was added in a fresh vial, and the reference measurement was repeated. After a brief equilibration period, the second reactant, PDA, was introduced. Then the sample interval was set 30 seconds. The reference measurements for dioxane and TFB were repeated before each experiment to avoid minor spectral shifts caused by restarting the laser and recalibrating the system.

The initial experiments were conducted with a lower concentration of 1 mg mL^{-1}, but it was observable after the first series of tests that this resulted in larger errors and no solid formed upon the addition of the catalyst. With increasing the concentration, we also performed measurements for a calibration line. Unfortunately, the intensity of the measurement varied a little, and peaks shifted a bit while the reaction occurred. This made it impossible to track the exact concentration during the reaction.

Nevertheless, with tracking the characteristic peaks over time it was still possible to get insight into the reaction progress. Several aspects of the reaction parameters were analysed with the Raman device, including the influence of mixing, temperature, ultrasonic energy input, and concentration.

To investigate the impact of mixing on the reaction, several experiments were conducted with a three-bladed impeller, which stirred the reaction solution at room temperature. The rotational speeds for the experiments were 200 rpm, 400 rpm, 600 rpm and no stirring. This series was performed with a concentration of 10 mg mL^{-1} of linker and linkage in dioxane.

Since the setup for the continuous reaction was carried out in an ultrasonic bath for mixing and better transport of the solids, an experiment with mixing in an ultrasonic bath was done. This was implemented by placing the vial in the ultrasonic bath for 2 minutes and measuring the reaction process via Raman spectroscopy after the mixing.

This was repeated 10 times to investigate a total reaction time of 20 minutes. Every experiment ended with adding the catalyst, 3 M acetic acid in water to the reaction solution forming solids and letting it rest for three hours.

With the new solvent system for the reaction, acetonitrile and a mixture of acetonitrile with imidazole, the reaction was again examined with the Raman device at different rotational speeds of 0 rpm, 200 rpm, 400 rpm, and 600 rpm. The concentration was set as in the dioxane experiments with 10 mg mL^{-1} of linker and linkage. The experiments using imidazole as solubility enhancement had a concentration of 20 mg mL^{-1} imidazole.

The formed COFs were then processed with the same downstream method as the G series of batch reactions since it had the best results.

The software Matlab was used to analyse and evaluate the gathered data from the experiments. The reaction rate and order were examined, and reaction time was assessed to estimate process parameters for the continuous flow experiments.

4.2.3. Continuous Flow Experiments

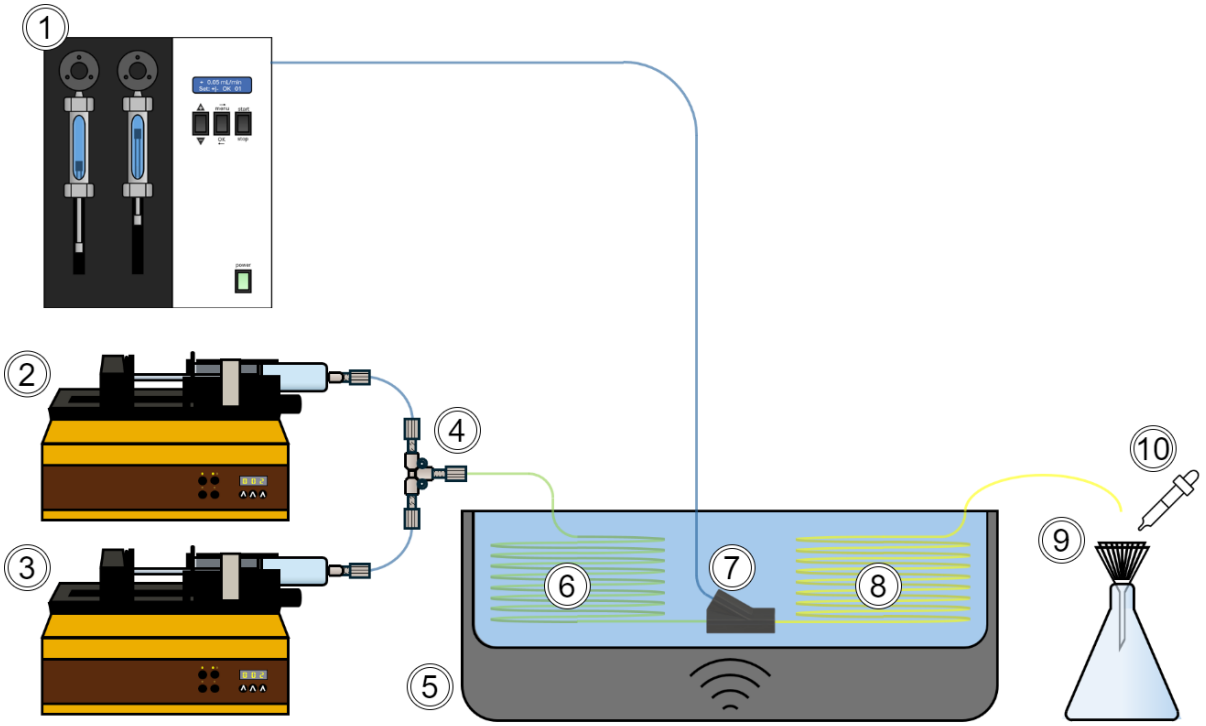

Figure 16: Continuous flow setup with (1) continuous syringe pump for the supply of the catalyst acetic acid, (2) & (3) conventional syringe pump with stainless steel syringes for the linker TFB and linkage PDA, (4) T – connector for mixing the reaction solution, (5) ultrasonic bath, (6) 1st section of the tubular reactor for the initial reaction, (7) 3D printed Y – connector to add the catalyst to the reaction solution, (8) 2nd section of the reactor for the formation of solids, (9) paper filter to separate the solids from liquid stream and (10) methanol to quench the reaction

With knowledge of well-performing batch process parameters, it was possible to design a continuous setup, which is shown in Figure 16. Concentration between 8 mg mL^{-1} to 16 mg mL^{-1} of the linker TFB and linkage PDA was tested to investigate the influence of the concentration on the flow setup. The tube length of the mixing part of the reactor was designed to meet the residence time of 15 min, which was determined from the Raman analysis.

At the end of this section, the catalyst acetic acid was added to the mixed reaction solution with a concentration of 1 M, 2 M, or 3M. At first, this was done with a standard T–connector, but this was one of the critical points for clogging, so it was later redesigned and 3D printed. The second part of the reactor was designed for a hydraulic residence time of 20 minutes, to give the solids enough time to be formed. The mixing part was submerged in the ultrasonic bath for each experiment, while the section containing the solid product, was tested with and without the influence of ultrasonic energy input.

Since clogging was always one of the biggest difficulties during the experiments several different pumps were used to overcome the back pressure. Furthermore, it was necessary to have a small and well-controlled flow rate of the reactants. The first tests were conducted with syringe pumps for the linker and linkage (TFB and PDA) in PP – syringes and an HPLC pump for the catalyst. The PP – syringes are not strong enough to withstand the force, which is necessary to generate such high pressures. Unfortunately, the HPLC pumps in our lab are not suited for such small flow rates as we need, with 0.05 mL min^{-1} per reactant stream. Another issue with the HPLC pumps was that they are unreliable if they are operated with different solvents and the solutions are frequently changed.

Therefore, the HPLC pump was replaced with a syringe pump, and the PP – syringes were replaced with stainless steel ones.

Furthermore, a slug flow approach was investigated since the clogging issue was still relevant for long-run experiments. The solvent dioxane is miscible with almost every other solvent; therefore, the slug flow was implemented with nitrogen as the second phase.

To finally solve the clogging problem, the syringe pump from Lambda which feeds the acetic acid into the system was replaced with a continuous syringe pump that can handle pressures up to 62 bar.

In

Table 2 the process parameters for each continuous flow experiment are listed.

Table 2: Overview of the different continuous flow experiments with dioxane as solvent

Exp. №	Pump Linker & Linkage	Pump Catalyst	Length 1st Section mm	Connector	Length 2nd Section mm	Concentration Linker & Linkage mg mL^{-1}	Concentration Acetic Acid	Flow Rate AA mL min^{-1}
1	Lambda 1 & 3	HPLC	5000	Stand. T	5000	10	3 M	0.2
2	Landgraf A	HPLC	5000	Stand. T	3000	16	3 M	0.2
3	Landgraf A	HPLC	5000	Stand. T	3000	16	3 M	0.2
4	Lambda 1 & 2	HPLC	5000	Stand. T	3000	16	3 M	0.2
5	Landgraf A	HPLC	5000	Stand. T	3000	16	3 M	0.2
6	Landgraf A	Lambda 2	5000	Stand. T	3000	16	3 M	0.2
7	Landgraf A	Lambda 2	5000	Stand. T	3000	16	3 M	0.2
8	Landgraf A	Lambda 2	5000	Stand. T	3000	16	3 M	0.2
9	Lambda 1 & 3	Lambda 2	2850	3D Y	3000	16	3 M	0.2
10	Landgraf A	Lambda 2	2850	3D Y	3000	16	3 M	0.2
11	Lambda 1 & 3	Lambda 2	2850	3D Y	3000	16	1 M	0.2
12	Lambda 1 & 3	Lambda 2	2850	3D Y	3000	8	1 M	0.2
13	Lambda 1 & 3	Lambda 2	2850	Stand. T	3000	8	3 M	0.2
14	Lambda 1 & 3	Lambda 2	2850	3D Y	3000	12	3 M	0.2
15	Lambda 1 & 3	Lambda 2	2850	3D Y	3000	12	3 M	0.2
16	Lambda 1 & 3	Lambda 2	2850	3D Y	3000	12	1 M	0.2
17	Lambda 1 & 3	Lambda 2	2850	3D Y	3000	12	1 M	0.2
18	Lambda 1 & 3	Lambda 2	2850	3D Y	3000	12	1 M	0.1
19	Lambda 1 & 3	Lambda 2	2850	3D Y	3000	12	1 M	0.1
20	Lambda 1 & 3	SyrDos	2850	3D Y	1500	12	1 M	0.05
21	Lambda 1 & 3	SyrDos	2850	3D Y	1500	12	3 M	0.05
22	Lambda 1 & 3	SyrDos	2850	3D Y	1100	12	3 M	0.01
23	Lambda 1 & 3	SyrDos	2850	3D Y	1100	12	1 M	0.01
24	Lambda 1 & 3	SyrDos	2850	3D Y	1100	12	2 M	0.01

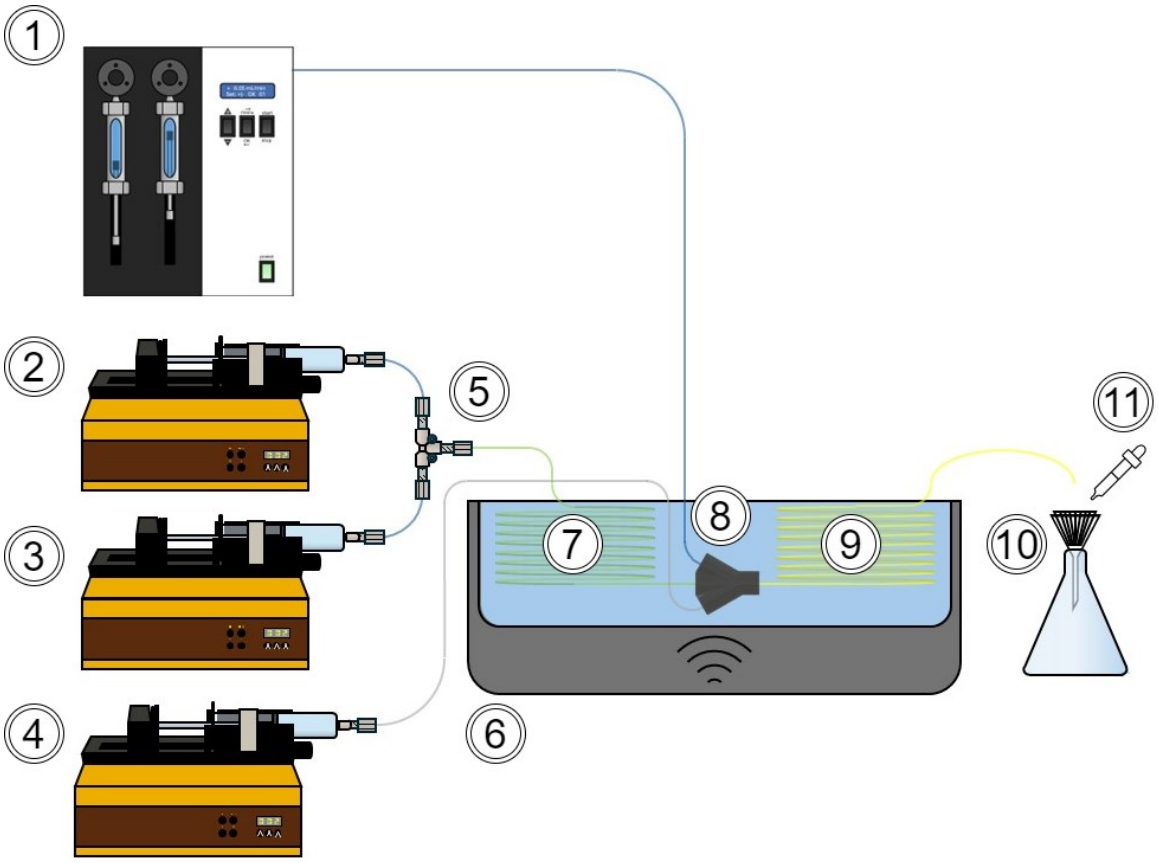

Figure 17: Continuous flow setup for a slug flow with (1) continuous syringe pump for the supply of the catalyst acetic acid, (2) & (3) conventional syringe pump with stainless steel syringes for the linker TFB and linkage PDA, (4) pump for the hexane or respectively mass flow controller for the N_2 (5) T – connector for mixing the reaction solution, (6) ultrasonic bath, (7) 1st section of the tubular reactor for the initial reaction, (8) 3D printed Y – connector to add the catalyst to the reaction solution and another phase for the slug flow, (9) 2nd section of the reactor for the formation of solids, (10) paper filter to separate the solids from liquid stream and (11) methanol to quench the reaction

The setup for slug flow experiments is depicted in Figure 17. At first, experiments with N_2 were performed with a concentration of linker and linkage of 16 mg mL^{-1}. The concentration of the catalyst acetic acid was 1 M or 3 M and fed with a flow rate of 0.2 ml min^{-1}. The N_2 stream varied from the lowest possible volumetric flow of 0.5 ml min^{-1} to 2 ml min^{-1}. At first, the N_2 feed was activated and after a stationary slug flow had formed, the acid was added. Overall, four experiments were carried out with nitrogen. Following this a series of experiments with acetonitrile as solvent was performed, since it's not miscible with hexane and enables another slug flow approach. To increase the solubility of the acetonitrile, imidazole was added with a concentration of 20 mg mL^{-1}. The concentration of linker (TFB) and linkage (PDA) was kept the same as in the last dioxane experiments with 12 mg mL^{-1} and fed with a flow rate of 0.05 mL min^{-1} for each stream. The acetic acid had a concentration of 2 M or 3 M and a flow rate of 0.01 mL

min^{-1} for the tests. Hexane was fed with 0.1 mL min^{-1} and as in the N_2 experiments, the slugs were formed before the acid was added. Continuous flow experiment 25 had a concentration of acetic acid of 3 M, due to clogging and a small sample size it was repeated as experiment 26. Experiment 27 had a concentration of 2 M acetic acid and the same flow rate.

5. Results and Discussion

5.1. Batch Reaction Covalent Organic Frameworks

Several batch experiments were already conducted in the preliminary work [68], but some results will be discussed here for comparison. All batch reactions yielded a solid product with a sponge-like texture and a light brown colour, with no visible differences between the samples when observed by the naked eye. However, significant disparities emerged during the first step of downstream processing, filtration. The vacuum filtration, assisted by a water jet vacuum pump, disrupted the sponge-like structure, breaking it into smaller particles suspended in the solvent. Drying the product in a desiccator under vacuum also negatively impacted its texture, as the rapid and uncontrolled release of solvent molecules caused the structure to degrade.

As a result, the samples V1, V2, and V3 exhibited very small surface areas that were too low to measure and had poor crystallinity. In contrast, the gentler work-up and solvent exchange procedures applied to samples G1, G2, and G3 resulted in significantly improved surface areas and crystallinity. Among these, G2 showed slightly better crystallinity than G3, but the surface area of G3 was much larger. This indicates that the ultrasonic treatment in dichloromethane, coupled with the longer reaction time, enhanced the crystallinity but negatively affected the surface area. Sample G1, however, performed the worst in both surface area and crystallinity measurements.

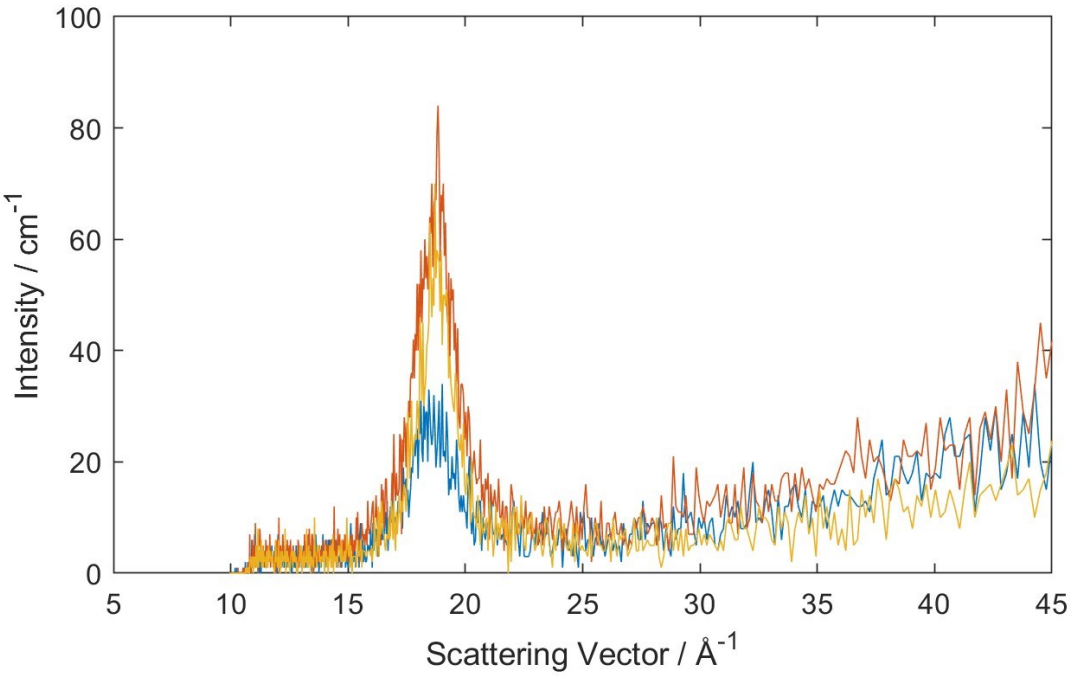

Figure 18: SAXS results of the samples G1, G2 and G3

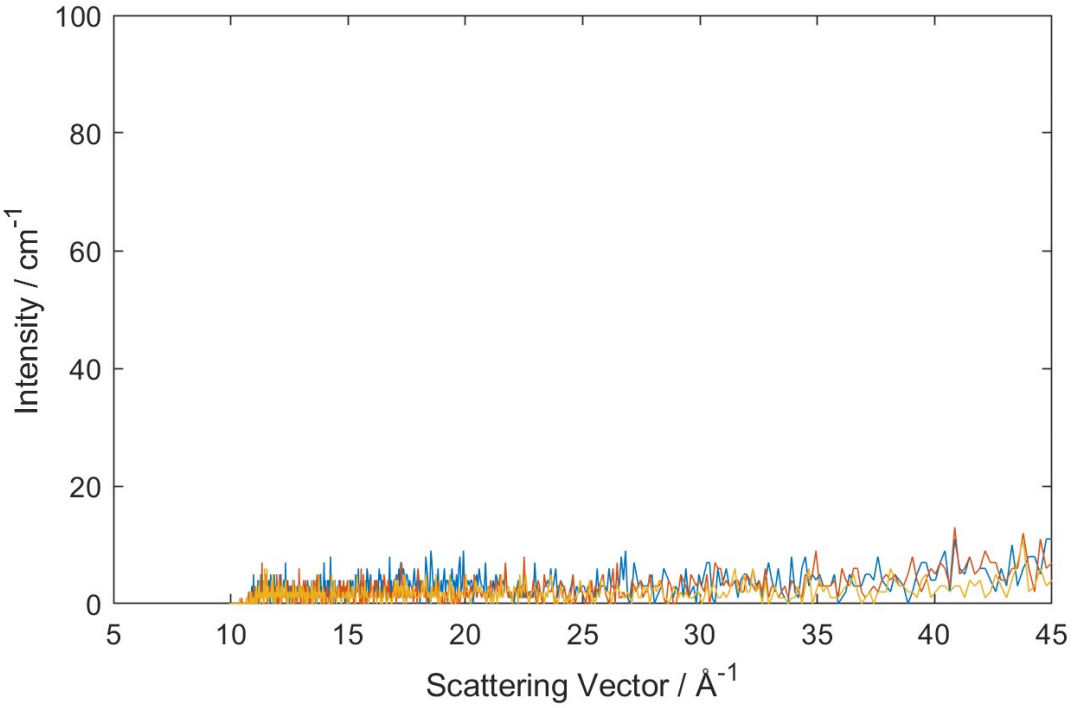

Figure 19: SAXS results of the samples V1, V2, and V3

Fehler! Verweisquelle konnte nicht gefunden werden. and **Fehler! Verweisquelle konnte nicht gefunden werden.** present the SAXS measurement results for samples G1, G2, and G3, as well as V1, V2, and V3. The G series samples exhibit a peak at 18.8 $Å^{-1}$, while the V series samples show no noticeable peak, indicating a clear difference in crystallinity between the two groups.

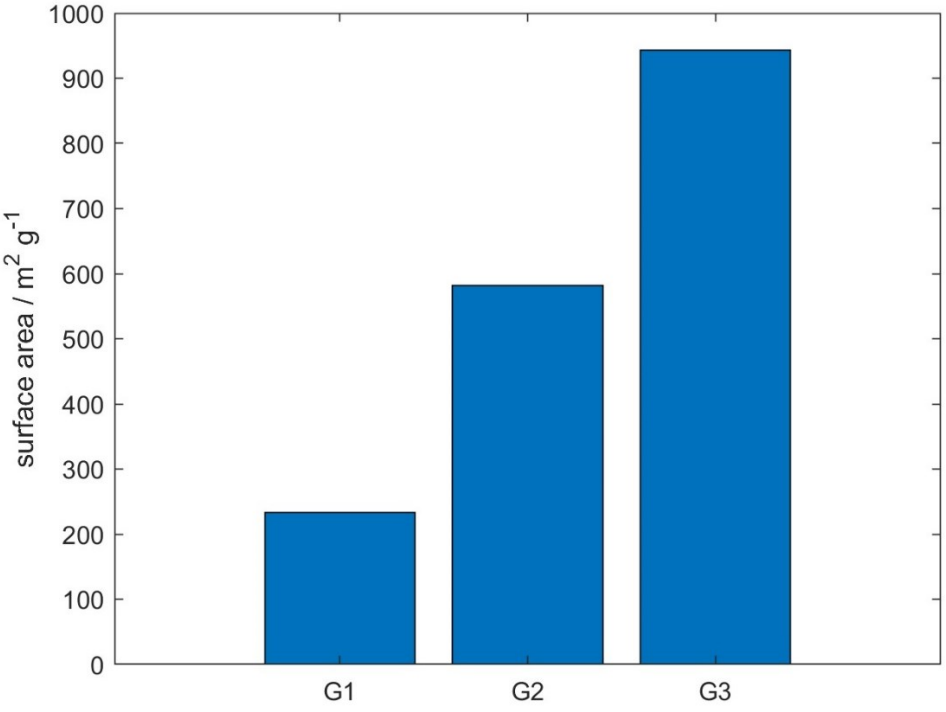

Figure 20: Surface area of the sample G1, G2 and G3

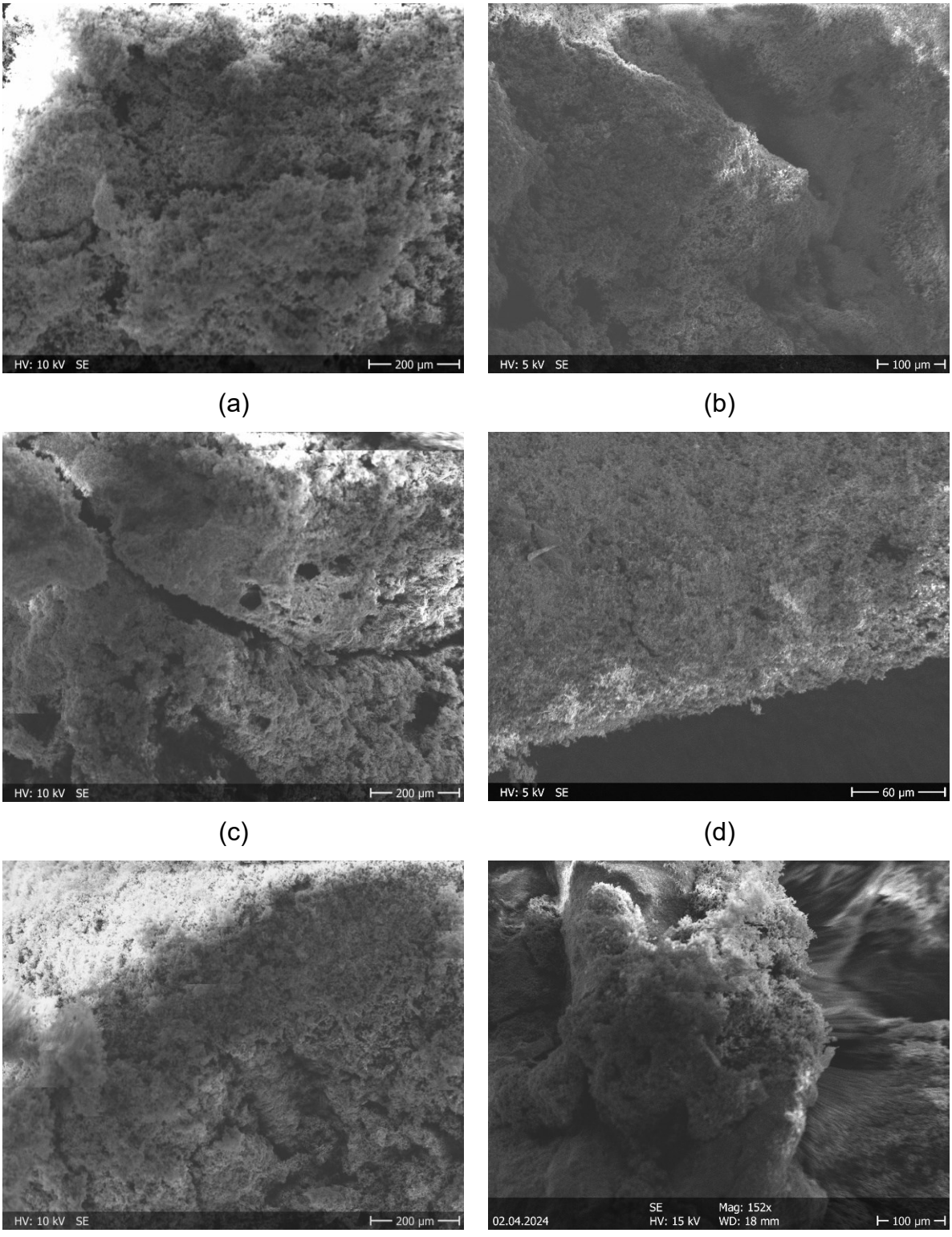

Figure 21: SEM picture of (a) G1 with 100x magnification, (b) V1 with 150x magnification, (c) G2 with 100x magnification, (d) V2 with 350x magnification, (e) G3 with 100x magnification, and (f) V3 with 150x magnification

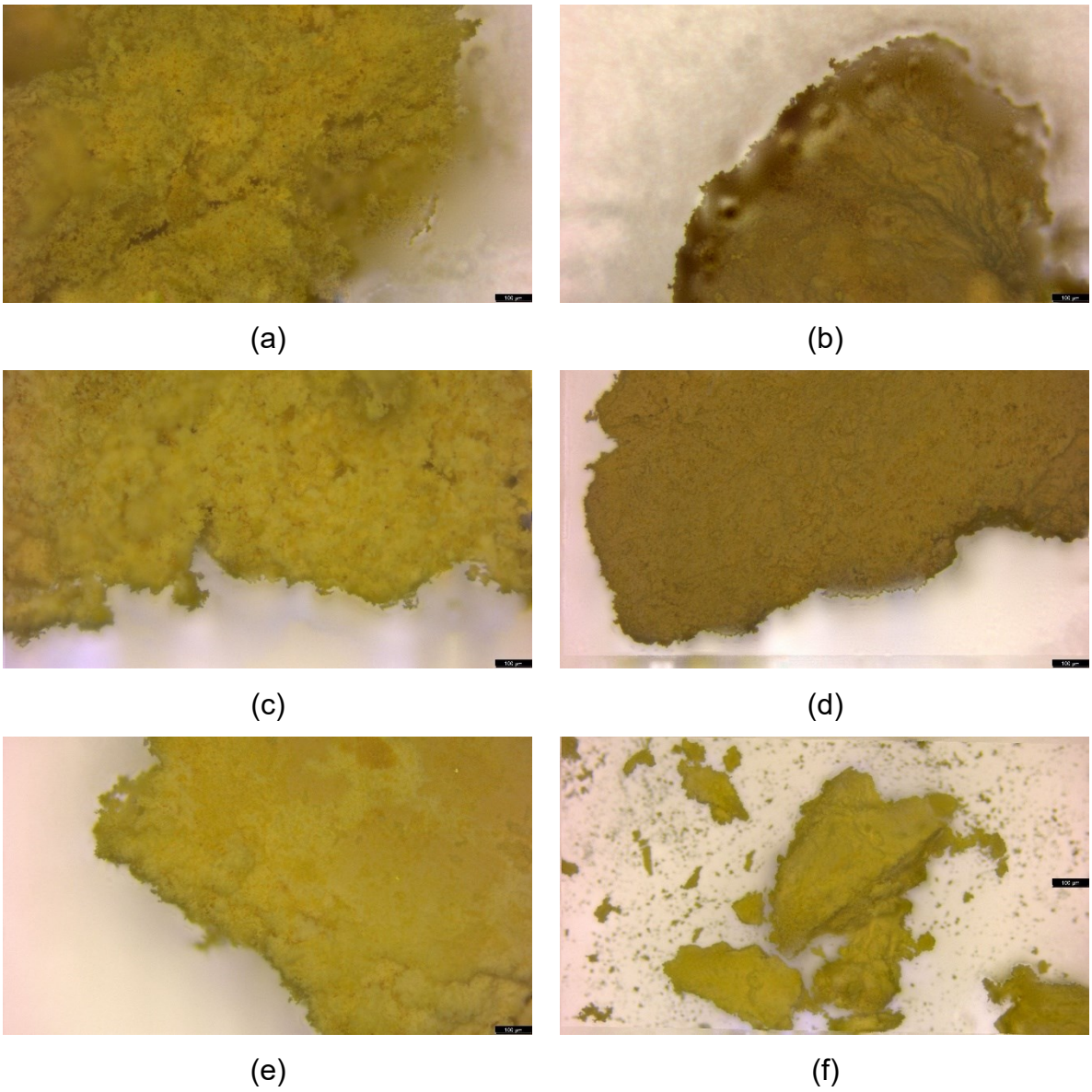

Figure 22: Optical microscope picture of (a) G1, (b) V1, (c) G2, (d) V2, (e) G3, and (f) V3 with a 100 µm scale bar

The difference in surface structure between the G and V series can be observed in the images captured using electron and optical microscopes, as shown in **Fehler! Verweisquelle konnte nicht gefunden werden.**. The G series products exhibit a visibly more porous surface compared to the V series, suggesting that the interior of the solids in the G series also possesses a more porous structure. However, the resolution of the electron microscope images was limited due to charging effects. Charging caused the sample to move under the influence of the electric fields, which hindered the stable focusing of the electron beam and reduced the achievable resolution.

Fehler! Verweisquelle konnte nicht gefunden werden. Figure 22 presents optical microscope images of the same products. The V series samples again show a less

porous surface, with a darker brownish colour, indicating differences in the texture and structure compared to the G series samples.

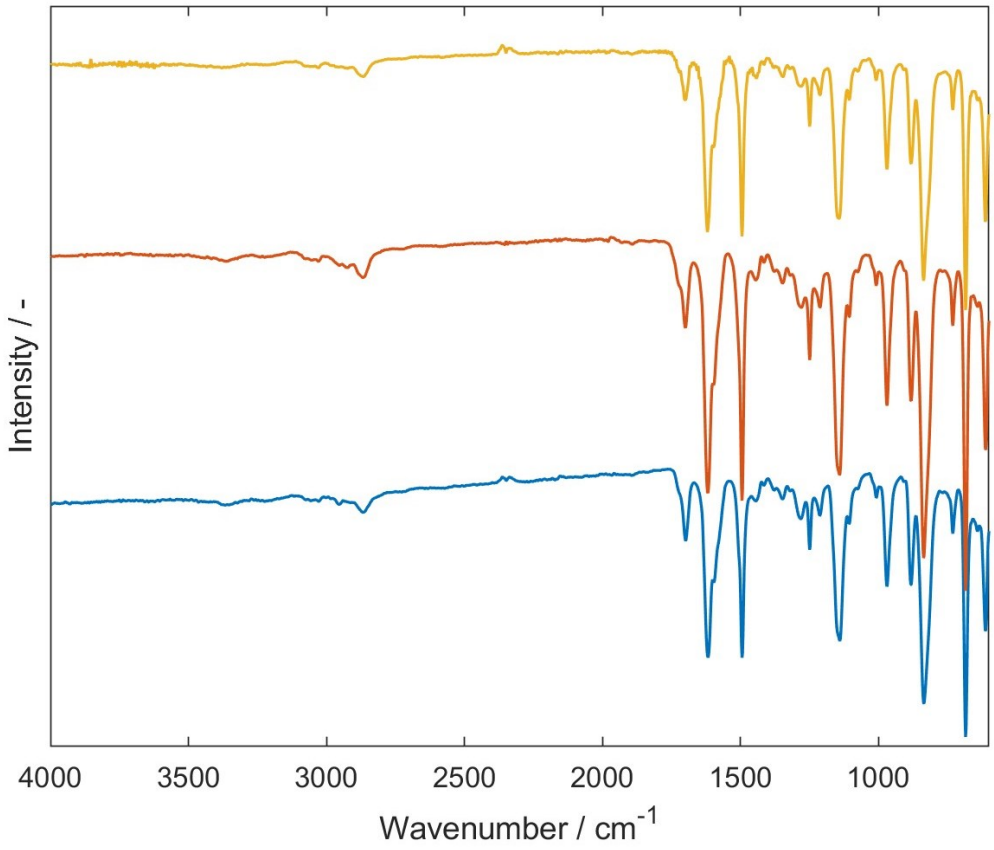

Figure 23: FTIR spectrum of G1 G2 and G3

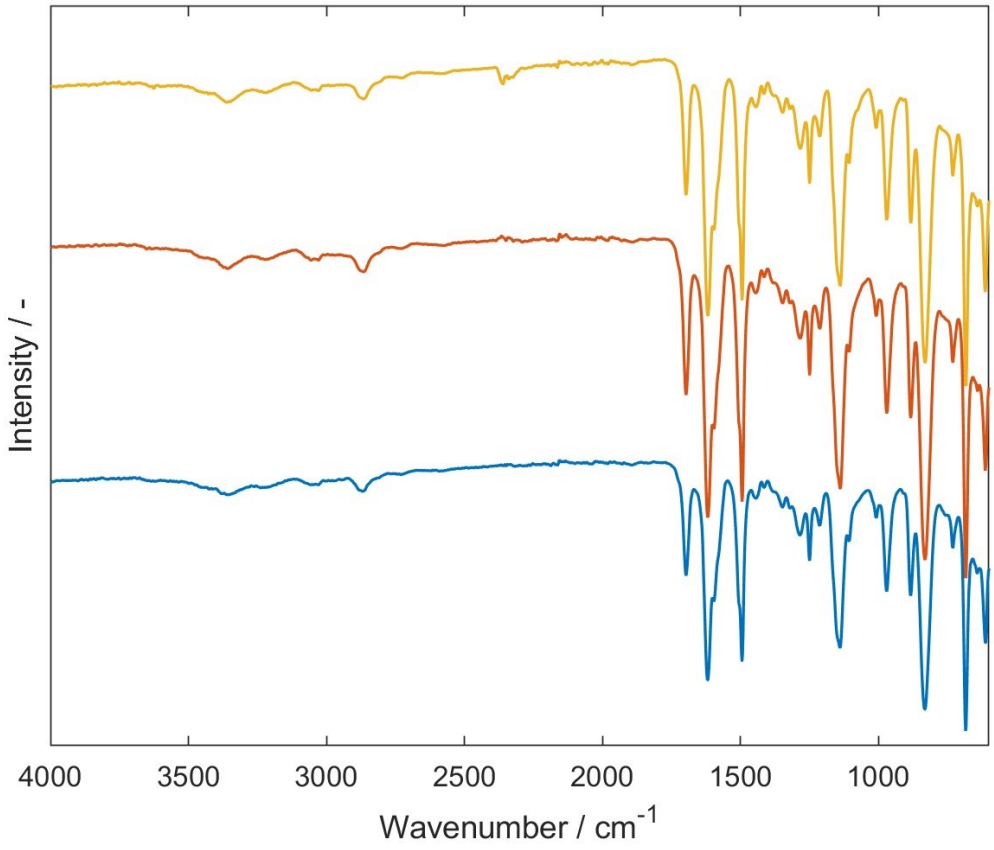

Figure 24: FTIR spectrum of V1 V2 and V3

The Fourier-transform infrared spectroscopy (FTIR) analysis of the G series samples showed no significant differences between them. However, additional peaks observed for G1 and G3 around a wavenumber of 2350 cm^{-1} suggest the presence of CO_2 in these samples. This CO_2 could have been introduced either during the synthesis process or as a result of storage and aging.

The spectra of V1, V2, and V3 are nearly identical to those of the G series, highlighting that the synthesis process is the same, with only the work-up procedure differing. Therefore, the observed differences in surface area, crystallinity, and morphology are primarily attributed to the variations in the work-up methods, such as filtration, solvent exchange, and drying procedures. These differences in processing appear to have a significant impact on the final properties of the products.

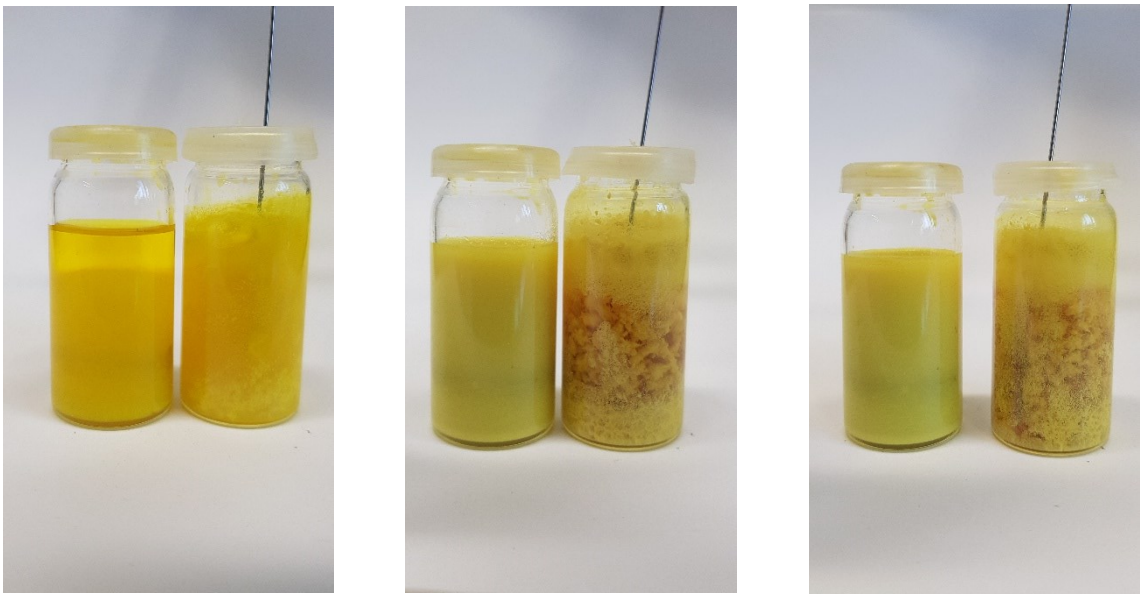

(a) (b) (c)

Figure 25: Repetition of the G3 experiment (left) and N2 experiment (right) at (a) 5 minutes of reaction (b) 1h of reaction (c) 2h of reaction

In the final batch experiment, G3 was repeated with and without a nitrogene stream. The surface area of the sample without N_2 was 1365.35 m^2 g^{-1} and for the experiment with N_2, the surface area was 1111.26 m^2 g^{-1}. This means that the disturbance from the nitrogen bubbles has more negative influence than the possible positive impact of lowering the oxygen saturation in the reaction solution

5.2. Raman Experiments

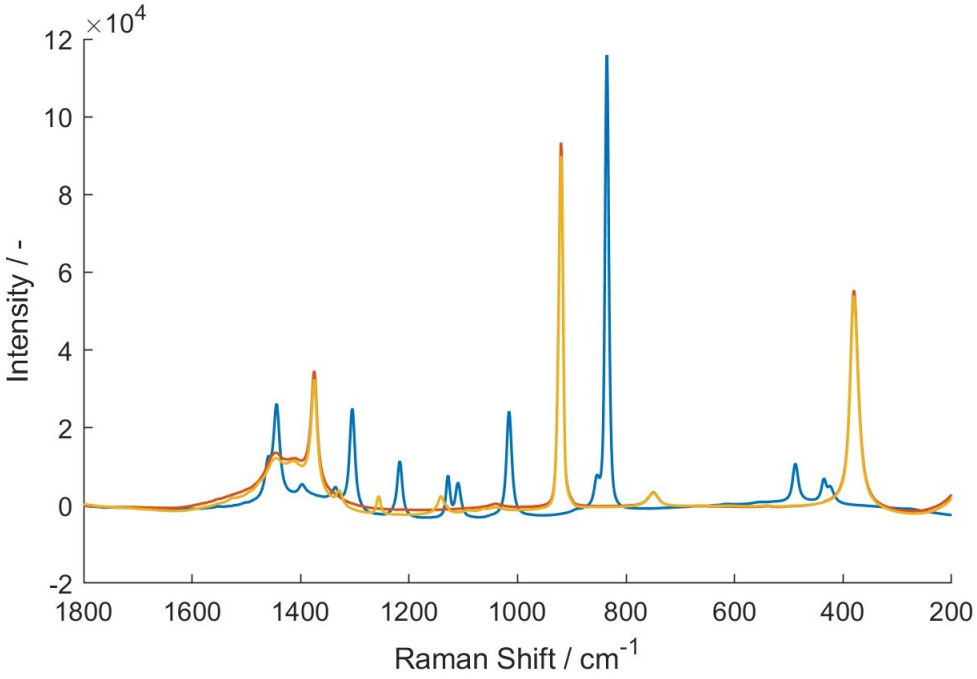

Figure 26: Spectrum of the different solvent systems; dioxane, acetonitrile and acetonitrile with 20 mg mL^{-1} imidazole

At the beginning of the experiments, Raman spectra of the solvents were recorded, as shown in Figure 26. These spectra were used as references and subtracted from all subsequent spectra. One can see that the imidazole adds a few peaks to the spectrum of the acetonitrile and none of the peaks overlap with the dioxane. The Pearson correction was applied to all recorded spectra to achieve a flat baseline.

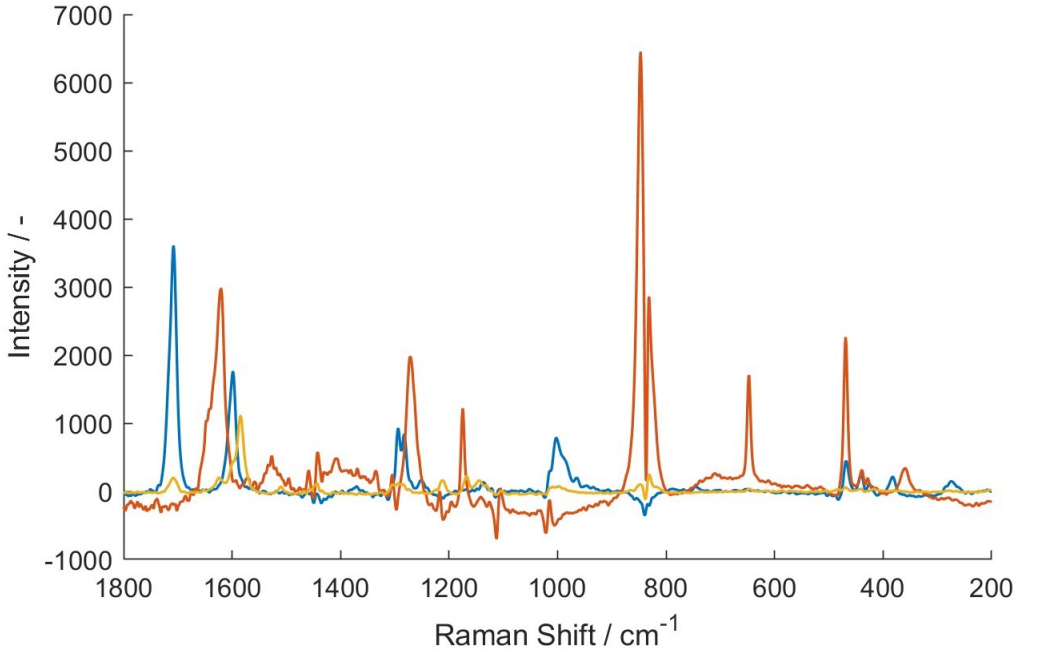

Figure 27: Spectra of linker (TFB), linkage (PDA) and product (COF)

Figure 27 displays the spectra of the linker (TFB), the linkage (PDA), and the resulting COF product. Especially, TFB exhibits a significant peak that does not overlap with any

other signal, observed at a Raman shift between 1740 and 1690 cm^{-1}. This makes it particularly suitable for monitoring the reaction progress, as its intensity decreases during the reaction. Additionally, a prominent peak characteristic of the COF appears between 1590 and 1550 cm^{-1}, which increases as the reaction advances. The spectra was compared to the literature and the significant peaks are the same. [69]
As mentioned, with the significant peaks, the reaction progress can be monitored. This made it possible to investigate the influence of process parameters like the mixing intensity on the reaction.

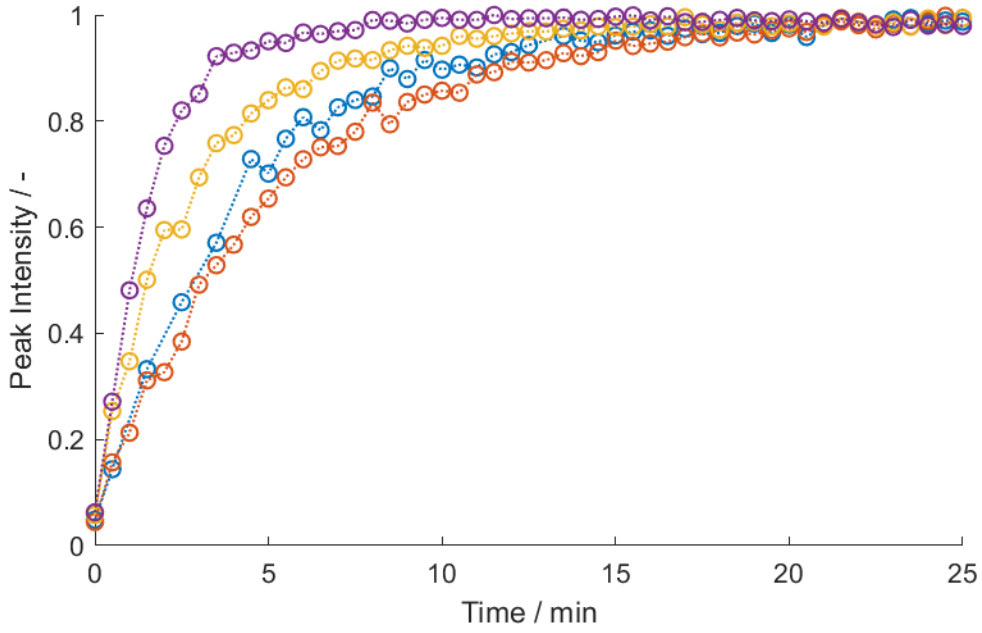

Figure 28: COF peak, solvent dioxane with a concentration of linker and linkage of 10 mg mL^{-1}; 0 rpm, 200 rpm, 400 rpm and 600 rpm

In Figure 28 the formation of the COFs is displayed over time for the different rotational speeds of 0 rpm, 200 rpm, 400 rpm, and 600 rpm in dioxane. The concentration of the linker and linkage is 10 mg mL^{-1}, and the reaction is carried out at room temperature. It is visible that with stronger mixing, the reaction is quicker. The curve of 200 rpm is flatter than the one with no stirring at all. This is likely because, at 200 rpm, the mixing is so weak that it has no noticeable impact on the reaction. Instead, the initial mixing that inevitably occurs when the second reactant is added plays a more decisive role. The peak intensity is normalized for the diagrams and spectra are treated with SNV (standard normal variate) scattering correction.

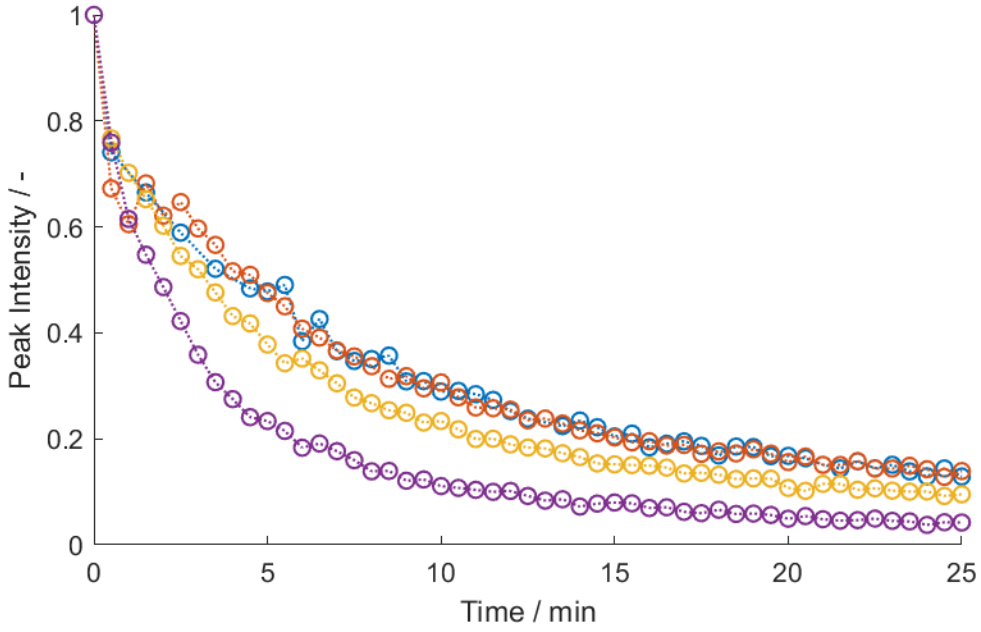

Figure 29: TFB peak, solvent dioxane with a concentration of linker and linkage of 10 mg mL^{-1}; 0 rpm, 200 rpm, 400 rpm, and 600 rpm

Figure 29 shows the decrease of the characteristic peak between 1740 and 1690 cm^{-1}. of TFB over time during the reaction. This again demonstrates that higher stirring rates have a positive effect on the reaction kinetics. At 200 rpm, the reaction shows no effective stirring, with the data points nearly overlapping with the ones without stirring, which confirms the previously stated assumption.

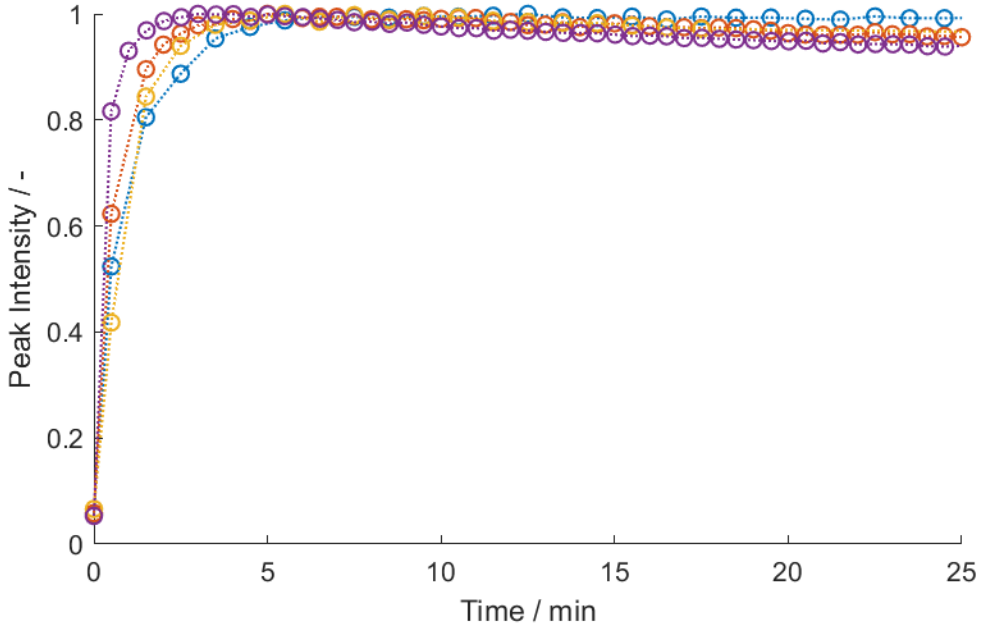

Figure 30: COF peak, solvent dioxane with a concentration of linker and linkage of 10 mg mL^{-1}; 0 rpm, 200 rpm, 400 rpm, and 600 rpm

The changing of the solvent for the reaction significantly impacted the reaction kinetics. One can see that in Figure 30 the formation of the product is a lot faster than in the experiments with dioxane.

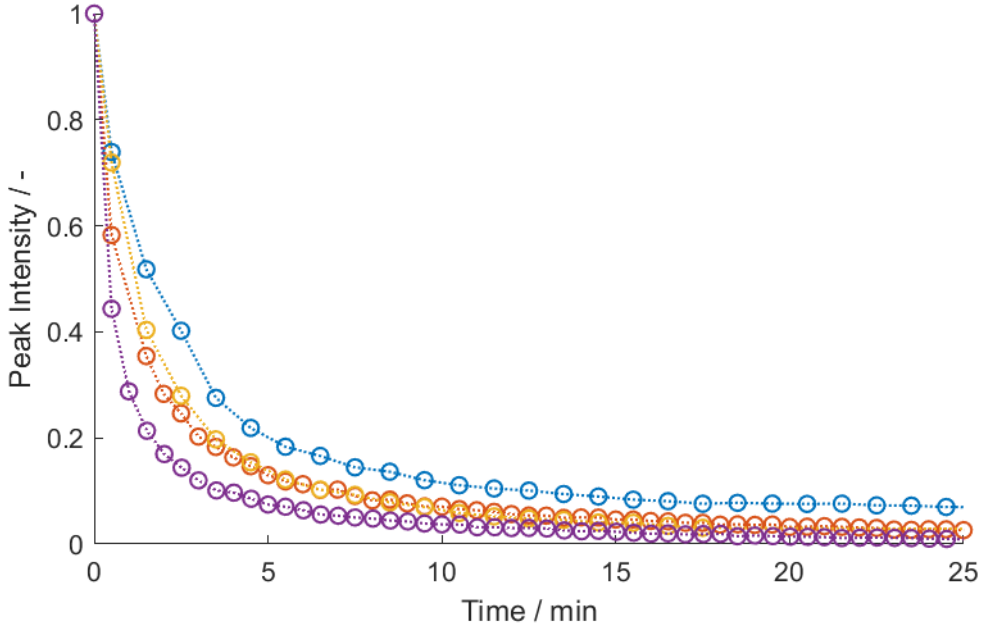

Figure 31: TFB peak, solvent acetonitrile with a concentration of linker and linkage of 10 mg mL^{-1}; 0 rpm, 200 rpm, 400 rpm, and 600 rpm

The same result is shown in Figure 31 for the TFB peak. The reaction was faster for every agitation level than in dioxan and mixing had a positive influence on the reaction time. The concentration of linker and linkage was the same as in the dioxane experiments.

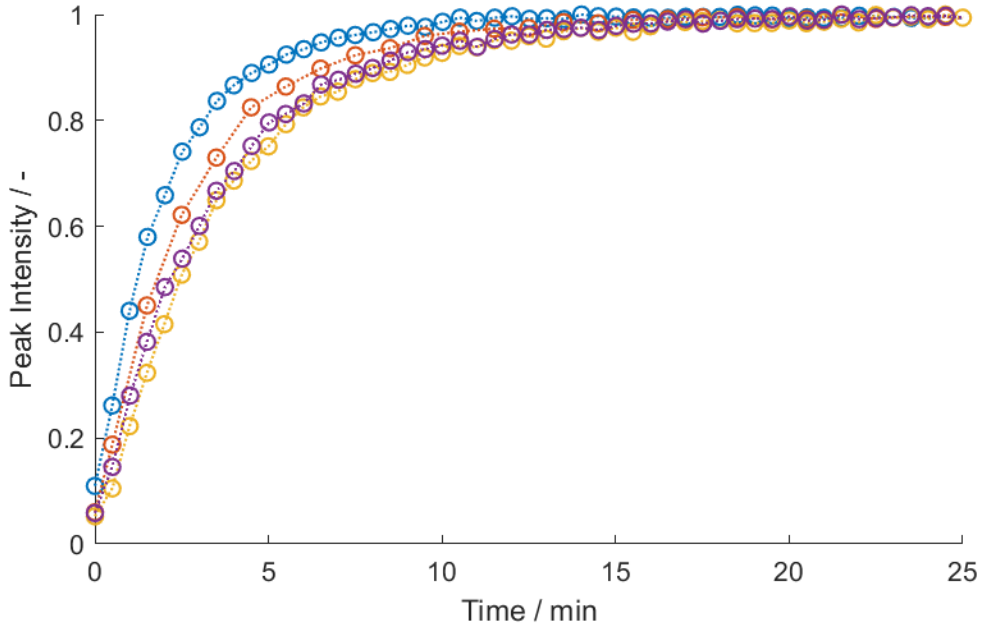

Figure 32: COF peak, solvent acetonitrile with 20 mg mL-1 imidazole and a concentration of linker and linkage of 10 mg mL-1; 0 rpm, 200 rpm, 400 rpm, and 600 rpm

In contrast, experiments using imidazole dissolved in acetonitrile as a solvent system exhibited slower reaction kinetics. Additionally, stronger stirring inhibited the reaction progress, as shown in Figure 32.

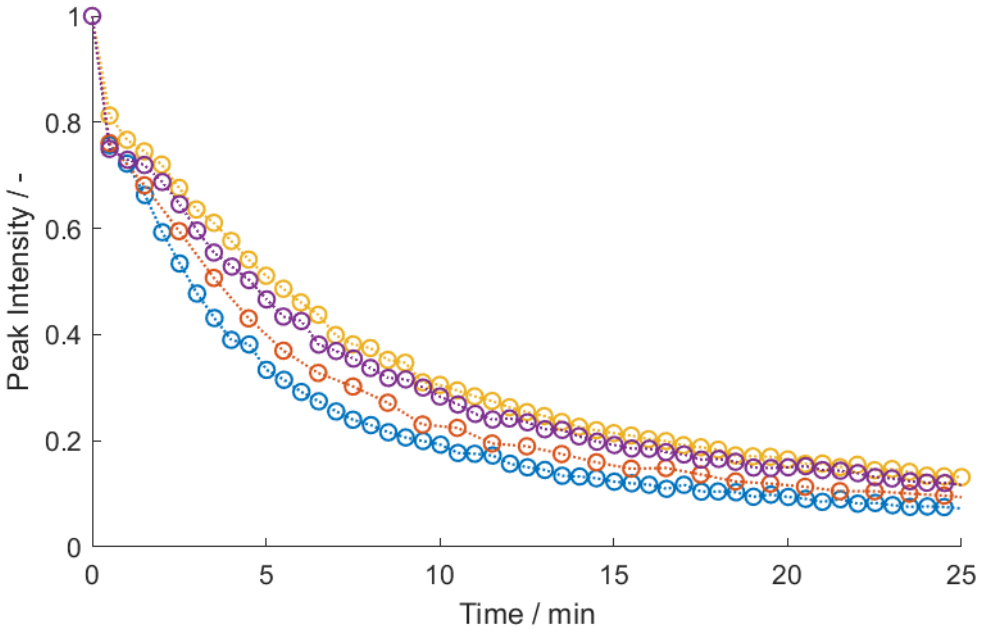

Figure 33: TFB peak, solvent acetonitrile with 20 mg mL^{-1} imidazole and a concentration of linker and linkage of 10 mg mL^{-1}; 0 rpm, 200 rpm, 400 rpm, and 600 rpm

Figure 33 depicts the same outcome for the TFB peak, confirming the other result.

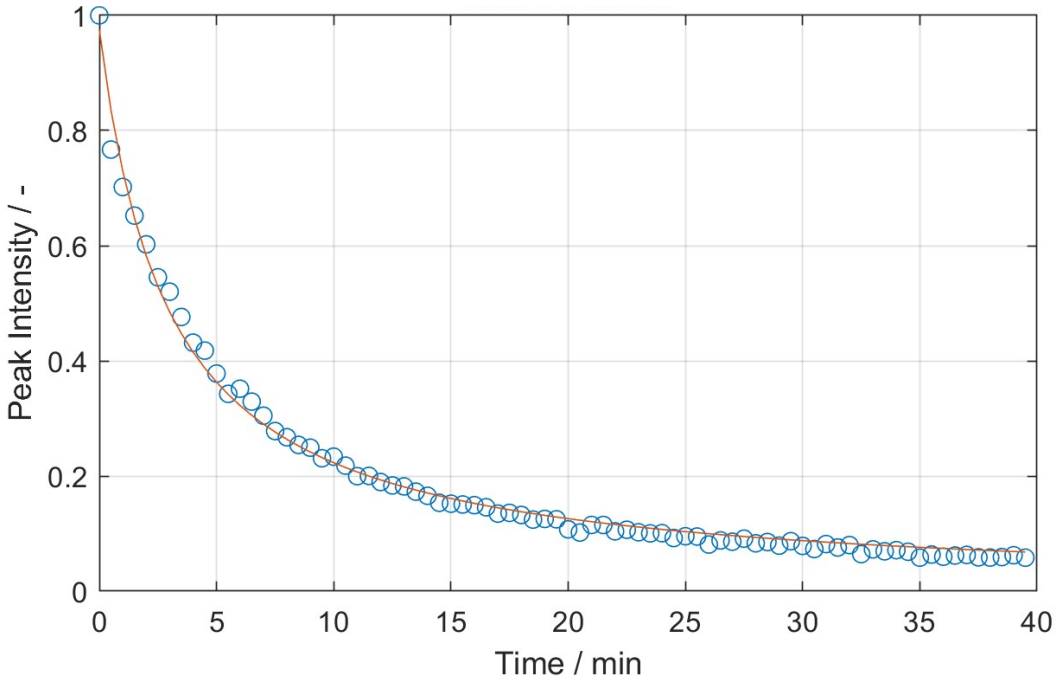

Figure 34: Normalized intensity over time with ○ the measured data points of the TFB peak and — the fit for reaction order 2 with 400 rpm agitating

To enable not only a graphical comparison of the reactions but also a quantitative analysis, the reaction kinetics were determined. This included calculating the reaction order as well as the reaction rate constant. In Figure 34, the experiment conducted at 400 rpm is shown as an example, where a fit for the reaction order and the reaction rate constant were applied to the experimental data points. Since the concentration of the educts or products can be measured with the SNV scattering correction, this calculation is just for this reaction parameters. The best fit was selected based on the R^2 value, ensuring the most accurate representation of the data. In

Table 3 the reaction rate constants and R^2 values for each experiment are listed. The reaction order was 2 for every experiment.

Table 3: Results of the analysis of the reaction kinetics in dioxane, acetonitrile and acetonitrile with 20 mg mL^{-1} imidazole

Solvent	Rotational Speed rpm	Rate Constant $AU^{-1}\ s^{-1}$	R^2
Dioxane	0	$3.94 \cdot 10^{-3}$	0.9816
	200	$3.90 \cdot 10^{-3}$	0.9682
	400	$5.76 \cdot 10^{-3}$	0.9936
	600	$7.16 \cdot 10^{-3}$	0.9841
Acetonitrile	0	$1.14 \cdot 10^{-2}$	0.9950
	200	$2.19 \cdot 10^{-2}$	0.9989
	400	$1.83 \cdot 10^{-2}$	0.9915
	600	$4.11 \cdot 10^{-2}$	0.9998
Acetonitrile Imidazole	0	$6.98 \cdot 10^{-3}$	0.9902
	200	$5.64 \cdot 10^{-3}$	0.9890
	400	$3.94 \cdot 10^{-3}$	0.9866
	600	$4.31 \cdot 10^{-3}$	0.9853

For some experiments, the R^2 value has a bigger deviation from 1, this is due to the initial unintended mixing when adding the linkage PDA to the linker TFB that is already in the vial. This results in a faster reaction in the first few seconds before it settles and matches the fit. When comparing the rate constants, you can see that the assumption based on the diagrams is correct and that the stronger mixing accelerates the formation

of the product in dioxane and pure acetonitrile. In contrast, mixing reduces the reaction rate in the acetonitrile imidazole solution.

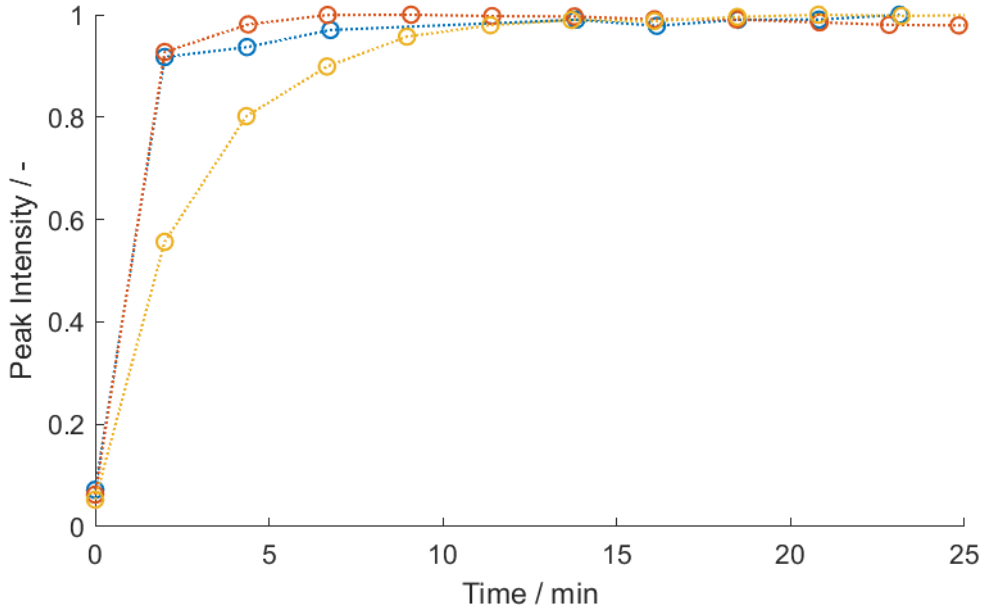

Figure 35: Progress of the reaction in different solvent systems with ultrasonic mixing following the COF peak: dioxane, acetonitrile, and acetonitrile with imidazole 20 mg mL^{-1}

Table 4: Reaction rate constants and R^2 of the reaction with ultrasonic mixing in different solvent systems

Solvent	Rate Constant $AU^{-1}\ s^{-1}$	R^2
Dioxane	$4.65 \cdot 10^{-2}$	0.8538
Acetonitrile	$4.85 \cdot 10^{-2}$	0.9638
Acetonitrile Imidazole	$6.96 \cdot 10^{-3}$	0.9607

The reaction kinetics of the experiment with the sonicated mixing are listed in Table 4. The reaction order is 2 for all solvents. The diagram of COF peak analysis is shown in Figure 34 and compares the different solvent systems to each other. One can see that the imidazole is unfavourable for the reaction, as in the stirred mixing reaction experiments. Due to the limited measurement steps of 2 minutes, the R^2 value deviates from 1, especially in the reaction with dioxane as solvent.

The reaction rates with ultrasonic mixing are comparable with the rates of mixing at 600 rpm. Experiments at high stirring speeds were not possible because the stirrer

became unsteady, posing a risk of damaging the equipment. Only dioxane has even better results with ultrasonic mixing than conventional mixing.

(a) (b) (c)

Figure 36: Progress of the reaction: (a) a few seconds after the catalyst was added, (b) after 10 minutes, (c) after three hours, shortly before the reaction was quenched

The Raman analysis ended with adding the catalyst, due to the interfering of formed solids on the measured spectra. The progress of the formation of the solid product is depicted in Figure 36. One can see that the COFs are growing from the bottom to the top and form a turbid suspension that solidifies over time to a spongelike body.

5.3. Continuous Flow Experiments

In the continuous flow experiments, two main aspects were analysed. First, the process feasibility was evaluated to determine whether the setup allowed steady-state operation and if this could be maintained over the entire experimental duration. Second, the properties of the resulting products were analysed using BET and SAX measurements to obtain information about the surface area and crystallinity.

The first few attempts used tubes with an inner diameter of 0.8 mm and a length of 5000 mm for each section. These trials had no ultrasonic mixing but included a static mixer. With a flow rate of 0.05 ml min^{-1} for each stream the hydraulic residence timer for the first section is 25:51 minutes. The manual verification resulted in a residence time of 23:43 to 25:16 minutes. The variation of the time is due to the slight variation of the pumps because we tried different brands of syringe pumps, and the error from manually recording the time it takes for the fluid to pass through the reactor.

The second segment had a hydraulic residence time of 8:23 minutes.

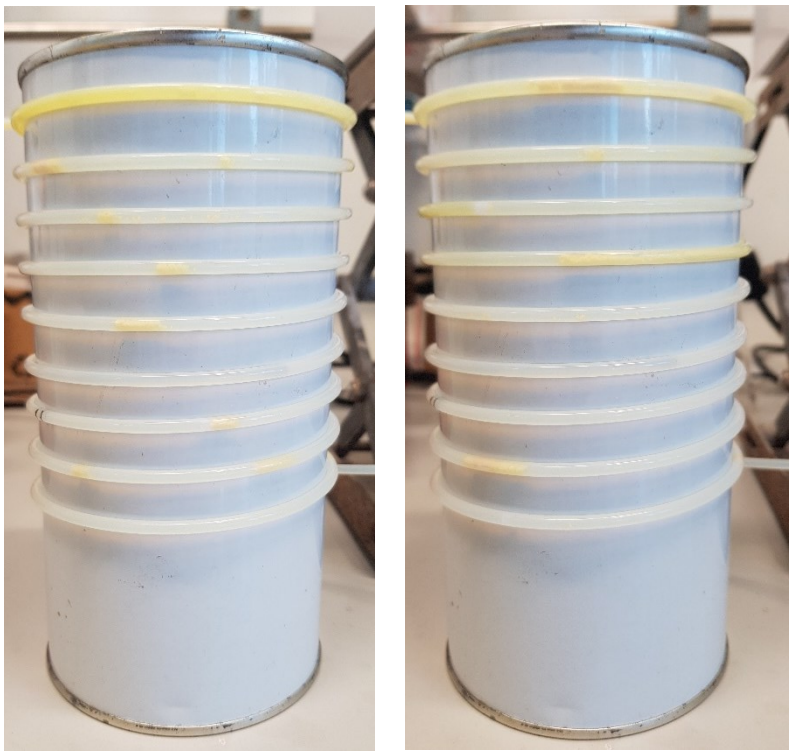

(a) (b)

Figure 37: Tubular reactor coiled around tin can as support. Movement of agglomerations (a) big agglomeration forming in first turn of the coil (b) agglomerate moved to the fourth turn

Due to clogging in the second section by solid bodies, the diameter of this section was increased. Consequently, the length of this section was reduced to 3000 mm resulting in a longer hydraulic residence time of 20:06 minutes. The manually recorded residence time for this section varied from 19:03 minutes to 21:09 minutes with some outliers.

Figure 37 shows the second section of the tubular reactor with an inner diameter of 1.6 mm where the solids are formed. One can see the movement of the product agglomerates. The formation of agglomerates in the tube leads to increasing backpressure and the gradual formation of blockages. Until the 6th continuous flow experiment the HPLC pump suppled the reaction system with the catalyst, acetic acid, but due to its inaccuracy and unreliability, it was replaced with a syringe pump. The HPLC pump was only further used o unclog the system once it was blocked by the formed solids. At this point we also started to submerge the whole system in an ultrasonic bath, to improve the mixing in the first section and flow of solids in the second section. The T - connector, which merges the reaction solution with the acetic acid was still one of the crucial parts of the setup in terms of clogging. Therefore, the self-design and 3D printed Y - connector was implemented, with an modified angle and diameter, to reduce the fouling at the transitions between the different parts and sections.

Due to the improved knowledge of the reaction from the Raman analysis, the first section was reduced to 2850 mm to match a hydraulic residence time of 15 minutes. In the manual verification a residence time is 14:21 to 16:03 minutes.

Despite the changes, the system still tended to clog at longer runtimes of the process. Therefore, the setup was changed to a segmented flow with nitrogen in the second section. The flow was divided into mostly uniform segments until the solid phase of the stream reached a critical ratio. The main issue with this setup was the lab's gas system pressure reducer, which was limited to 8 bars. As backpressure increased due to solid formation and fouling, the gas flow was restricted.

Consequently, the original setup was reconstructed and the size of the syringe for the acetic acid stream was reduced to increase the pressure. The downside of the smaller syringe was that the syringe had to be refilled during the process. This resulted in a pause of the stream for about one minute and a restart phase of another 20 seconds until the present back pressure was overcome. This pause increased the risk of clogging dramatically.

This problem was finally solved when the continuous syringe pump was implemented for the catalyst stream. The high pressure of this pump enables the release of arising blockages. Furthermore, the issue of refilling the acetic acid syringe was also no longer relevant. With these changes, a continuous operation was feasible for more than three hours, and ended due to the limited volume of the stainless steel syringes.
Finally, the slug flow approach was attempted again, but this time with two liquid phases, instead of a gaseous and liquid phase. This was possible due to the change of solvent for the reaction. Acetonitrile enables a slug flow with hexane, which is already used in the postprocessing routine. This setup showed a improved formation of slugs to transport small solid agglomerate. Unfortunately, if they reached a bigger size, they still got stuck in the tube until more particles agglomerated. The agglomerate size increase until the whole circumstance of the tube was blocked. If this state was reached whole solid plug was pushed through the tube. At this point, it was impossible the maintain the slug flow.

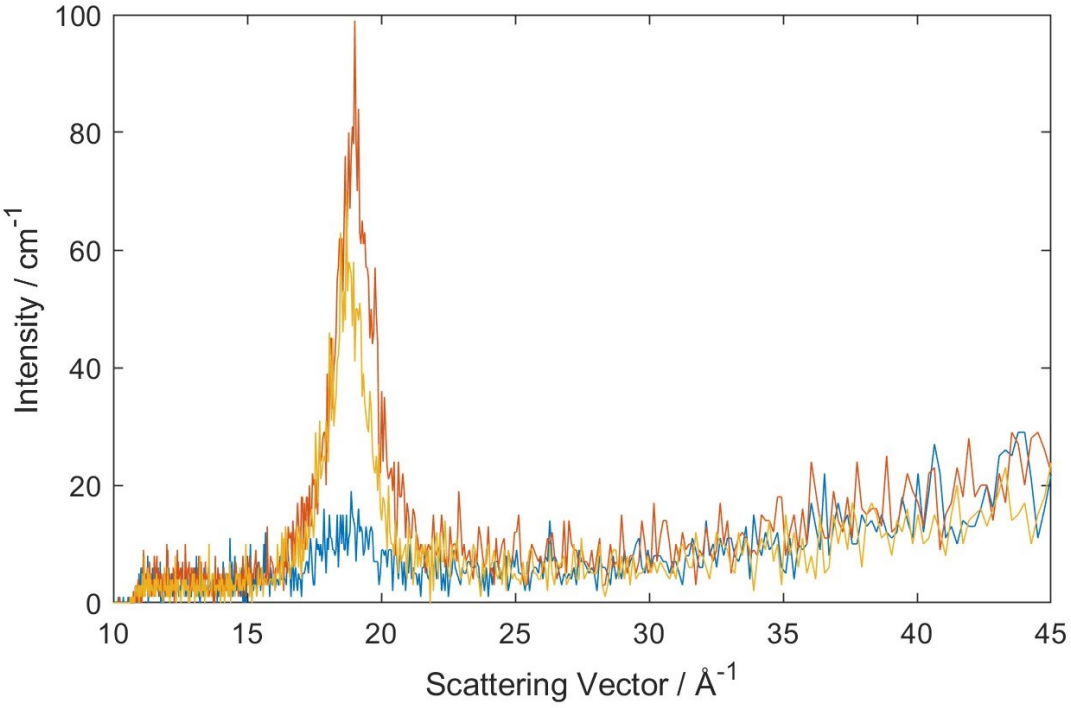

Figure 38: SAX measurements: continuous flow experiment with N2 slug flow, continuous flow experiment 21 and batch experiment G3

The product gained from these experiments was analysed via SAX and BET as they are the main characteristics to assess the performance of these reactions. The measurements with the FTIR device showed in the studies with the batch reaction that the reaction procedure has no influence on these results.

With the SAX measurements it was shown that the continuous flow experiment number 21 was the most crystalline one, with a peak scattering intensity of 99 cm^{-1}. The other experiments resulted with no peak at all, or peaks between 17 cm^{-1} to 25 cm^{-1}. In Figure 38 the SAX results of the continuous flow experiment with the N_2 slug flow, experiment 21 and the batch experiment G3. This demonstrates that crystallinity and surface area are not directly correlated, as the G3 experiment and the N2 experiment exhibit significantly higher surface areas compared to experiment 21. The baseline noise is 10 cm^{-1}, meaning that these samples have a very weak crystallinity.
In Table 5 the SAX maximum peaks of the experiments with a measurable crystallinity are shown.

Table 5: SAX results

Experiment Number	Intensity cm^{-1}
12	17
13	19
20	25
21	99
22	19
23	26

The SAX measurement results are likely poor because several weeks passed between sample generation and measurement. Unfortunately, this delay was caused by the failure of the SAX measurement device. It was observed that the crystallinity decreases over time. The same applies to the surface area measured via BET; however, in that case, it was always possible to perform the analysis at short intervals. The deterioration of these properties in the COF may be due to oxidation by atmospheric oxygen. In later experiments, the products were therefore stored in an argon atmosphere until they were measured. The BET measurement results for the continuous experiments are moderately good. Most values range between a surface area of 26 and 56 $m^2\ g^{-1}$, with one outlier at 12.12 $m^2\ g^{-1}$ and a few exceeding 100 $m^2\ g^{-1}$, reaching nearly 300 $m^2\ g^{-1}$. The best result was obtained using the nitrogen slug flow setup with 453.92 $m^2\ g^{-1}$. However, it should be noted that this experiment performed poorly in terms of process feasibility. Compared with the best batch result with 1365.35 $m^2\ g^{-1}$, it is less

than 34% of the surface area. The individual results for the experiments that yielded sufficient sample material for the BET measurement are listed in Table 6. No clear trend can be observed in the results. The work-up procedure for each experiment was identical and therefore had little influence. The sample size remained constant, and the positioning of the tubes and the Y-connector was also very similar. The promising result from the N_2 experiment was repeated in batch mode to test whether N_2 had a positive effect on the formation of COF product. However, the batch experiment, conducted without N_2, showed better results.

Table 6: Results of the BET measurements

Experiment Number	Surface Area $m^2 g^{-1}$
3	128.92
4	87.68
6	56.42
8	295.95
10	48.97
12	26.99
14	101.84
15	48.27
17	282.71
19	29.71
20	24.62
21	40.8
22	34.65
23	26.66
24	35.73
26	12.12
27	28.75
N_2	453.92

6. Conclusions and Outlook

This study examined the feasibility of continuous flow synthesis for Covalent Organic Frameworks (COFs) and analysed key process parameters. Solvent choice, mixing conditions, and reaction time were found to influence COF formation, crystallinity, and surface area. Initial challenges such as clogging and inconsistent product formation were addressed by using slug flow techniques and ultrasonic mixing, which improved process stability and product quality.

Raman spectroscopy was used to monitor reaction kinetics, allowing better control of synthesis conditions. SAXS and BET analyses showed that process parameters affected structural and surface properties. The highest crystallinity was observed in a continuous flow experiment 21, with a SAXS peak scattering intensity of 99 cm^{-1}. Other experiments showed lower crystallinity, with peak intensities ranging from 17 cm^{-1} to 25 cm^{-1}. Surface area measurements varied, with the highest value in continuous flow synthesis reaching 453.92 m^2/g when using nitrogen slug flow. Most experiments resulted in surface areas between 26 and 56 m^2/g, which were lower than the highest batch experiment result of 1365.35 m^2/g.

Reaction kinetics analysis determined a second-order reaction in all cases. The rate constants varied with solvent and mixing conditions. In dioxane, the reaction rate increased with mixing, ranging from 3.94×10^{-3} $AU^{-1}s^{-1}$ without stirring to 7.16×10^{-3} $AU^{-1}s^{-1}$ at 600 rpm. In acetonitrile, the reaction rate was higher, reaching 4.11×10^{-3} $AU^{-1}s^{-1}$ at 600 rpm. The presence of imidazole in acetonitrile reduced the reaction rate, with values around 4.31×10^{-3} $AU^{-1}s^{-1}$ at 600 rpm. Ultrasonic mixing improved reaction kinetics particularly in dioxane. Slug flow using nitrogen or hexane helped reduce clogging but did not fully prevent blockages in long-term experiments. A continuous syringe pump was introduced to improve process stability, reducing clogging and enabling longer experimental runs.

Although continuous flow synthesis is feasible, further optimization is needed to achieve similar high crystallinity and surface area like obtained in batch synthesis. Future research should focus on improving reactor design to reduce clogging, testing alternative catalysts to enhance reaction efficiency, and exploring additional COF applications in separation and catalysis. Using Powder X-ray Diffraction (PXRD) would also improve the analytics in term of crystallinity compared to SAXS. For future work, it would be advisable to replace the tubular reactor with a Continuous Stirred-Tank Reactor (CSTR), which is mixing the reaction solution via a nitrogen showerhead. This

setup would promote better mixing throughout the reaction and the appearance of clogging would be minimized. Additionally, it has been observed that solids tend to adhere and agglomerate around mechanical stirrers, which could negatively impact the reaction efficiency and consistency.

Appendix A

List of figures

List of tables

List of references

[1] A.P. Côté, A.I. Benin, N.W. Ockwig, M. O'Keeffe, A.J. Matzger, O.M. Yaghi, Porous, crystalline, covalent organic frameworks, Science 310 (2005) 1166–1170. https://doi.org/10.1126/science.1120411.

[2] H. Fan, A. Mundstock, A. Feldhoff, A. Knebel, J. Gu, H. Meng, J. Caro, Covalent Organic Framework–Covalent Organic Framework Bilayer Membranes for Highly Selective Gas Separation, J. Am. Chem. Soc. 140 (2018) 10094–10098. https://doi.org/10.1021/jacs.8b05136.

[3] P. Kuhn, M. Antonietti, A. Thomas, Ionothermalsynthese von porösen kovalenten Triazin-Polymernetzwerken, Angewandte Chemie 120 (2008) 3499–3502. https://doi.org/10.1002/ange.200705710.

[4] C.R. DeBlase, K.E. Silberstein, T.-T. Truong, H.D. Abruña, W.R. Dichtel, β-Ketoenamine-Linked Covalent Organic Frameworks Capable of Pseudocapacitive Energy Storage, J. Am. Chem. Soc. 135 (2013) 16821–16824. https://doi.org/10.1021/ja409421d.

[5] M. Martínez-Fernández, E. Martínez-Periñán, A. de La Peña Ruigómez, J.J. Cabrera-Trujillo, J.A.R. Navarro, F. Aguilar-Galindo, D. Rodríguez-San-Miguel, M. Ramos, R. Vismara, F. Zamora, E. Lorenzo, J.L. Segura, Scalable Synthesis and Electrocatalytic Performance of Highly Fluorinated Covalent Organic Frameworks for Oxygen Reduction, Angew. Chem. Int. Ed Engl. 62 (2023) e202313940. https://doi.org/10.1002/anie.202313940.

[6] S.Y.-L. Chong, Synthesis of chemically stable covalent organic frameworks in water, IUCrJ 3 (2016) 391–392. https://doi.org/10.1107/S2052252516016900.

[7] R.W. Tilford, S.J. Mugavero, P.J. Pellechia, J.J. Lavigne, Tailoring microporosity in covalent organic frameworks, Adv. Mater. 20 (2008) 2741–2746. https://doi.org/10.1002/adma.200800030.

[8] R. Roy, A.M. Evans, Reproducibility challenges in activating two-dimensional polymers and three-dimensional covalent organic frameworks, Communications Materials 5 (2024) 102. https://doi.org/10.1038/s43246-024-00536-x.

[9] X. Feng, X. Ding, D. Jiang, Covalent organic frameworks, Chem. Soc. Rev. 41 (2012) 6010–6022. https://doi.org/10.1039/C2CS35157A.

[10] P. Martinez-Bulit, A. Sorrenti, D. Rodriguez San Miguel, M. Mattera, Y. Belce, Y. Xia, S. Ma, M.-H. Huang, S. Pané, J. Puigmartí-Luis, In flow-based technologies: A new paradigm for the synthesis and processing of covalent-organic frameworks, Chemical Engineering Journal 435 (2022) 135117. https://doi.org/10.1016/j.cej.2022.135117.

[11] R.-R. Liang, S.-Y. Jiang, R.-H. A, X. Zhao, Two-dimensional covalent organic frameworks with hierarchical porosity, Chem. Soc. Rev. 49 (2020) 3920–3951. https://doi.org/10.1039/D0CS00049C.

[12] B. Gui, G. Lin, H. Ding, C. Gao, A. Mal, C. Wang, Three-Dimensional Covalent Organic Frameworks: From Topology Design to Applications, Acc. Chem. Res. 53 (2020) 2225–2234. https://doi.org/10.1021/acs.accounts.0c00357.

[13] J. Hu, S.K. Gupta, J. Ozdemir, M.H. Beyzavi, Applications of Dynamic Covalent Chemistry Concept towards Tailored Covalent Organic Framework Nanomaterials: A Review, ACS Appl. Nano Mater. 3 (2020) 6239–6269. https://doi.org/10.1021/acsanm.0c01327.

[14] S. Dalapati, S. Jin, J. Gao, Y. Xu, A. Nagai, D. Jiang, An azine-linked covalent organic framework, J. Am. Chem. Soc. 135 (2013) 17310–17313. https://doi.org/10.1021/ja4103293.

[15] Y. Ren, S. Yang, Y. Xu, Crystalline Covalent Triazine Frameworks and 2D Triazine Polymers: Synthesis and Applications, Acc. Chem. Res. 58 (2025) 474–487. https://doi.org/10.1021/acs.accounts.4c00729.

[16] H. Zhuang, C. Guo, J. Huang, L. Wang, Z. Zheng, H.-N. Wang, Y. Chen, Y.-Q. Lan, Hydrazone-Linked Covalent Organic Frameworks, Angew. Chem. Int. Ed Engl. 63 (2024) e202404941. https://doi.org/10.1002/anie.202404941.

[17] Y. Peng, W.K. Wong, Z. Hu, Y. Cheng, D. Yuan, S.A. Khan, D. Zhao, Room Temperature Batch and Continuous Flow Synthesis of Water-Stable Covalent Organic Frameworks (COFs), Chemistry of Materials 28 (2016) 5095–5101. https://doi.org/10.1021/acs.chemmater.6b01954.

[18] K. Asokan, M.K. Patil, S.P. Mukherjee, S.B. Sukumaran, T. Nandakumar, Scalable Mechanochemical Synthesis of β-Ketoenamine-linked Covalent Organic Frameworks for Methane Storage, Chem. Asian J. 17 (2022) e202201012. https://doi.org/10.1002/asia.202201012.

[19] L.K. Ritchie, A. Trewin, A. Reguera-Galan, T. Hasell, A.I. Cooper, Synthesis of COF-5 using microwave irradiation and conventional solvothermal routes, Microporous and Mesoporous Materials 132 (2010) 132–136. https://doi.org/10.1016/j.micromeso.2010.02.010.

[20] L. Akyuz, An imine based COF as a smart carrier for targeted drug delivery: From synthesis to computational studies, Microporous and Mesoporous Materials 294 (2020) 109850. https://doi.org/10.1016/j.micromeso.2019.109850.

[21] S. Nath, A. Puthukkudi, J. Mohapatra, B.P. Biswal, Covalent Organic Frameworks as Emerging Nonlinear Optical Materials, Angew. Chem. Int. Ed Engl. 62 (2023) e202218974. https://doi.org/10.1002/anie.202218974.

[22] F. Haase, K. Gottschling, L. Stegbauer, L.S. Germann, R. Gutzler, V. Duppel, V.S. Vyas, K. Kern, R.E. Dinnebier, B.V. Lotsch, Tuning the stacking behaviour of a 2D covalent organic framework through non-covalent interactions, Mater. Chem. Front. 1 (2017) 1354–1361. https://doi.org/10.1039/C6QM00378H.

[23] J.S. de Vos, S. Borgmans, P. van der Voort, S.M.J. Rogge, V. van Speybroeck, ReDD-COFFEE: a ready-to-use database of covalent organic framework structures and accurate force fields to enable high-throughput screenings, J. Mater. Chem. A 11 (2023) 7468–7487. https://doi.org/10.1039/D3TA00470H.

[24] J. Xiao, J. Chen, J. Liu, H. Ihara, H. Qiu, Synthesis strategies of covalent organic frameworks: An overview from nonconventional heating methods and reaction media, Green Energy & Environment 8 (2023) 1596–1618. https://doi.org/10.1016/j.gee.2022.05.003.

[25] K. Geng, T. He, R. Liu, S. Dalapati, K.T. Tan, Z. Li, S. Tao, Y. Gong, Q. Jiang, D. Jiang, Covalent Organic Frameworks: Design, Synthesis, and Functions, Chem. Rev. 120 (2020) 8814–8933. https://doi.org/10.1021/acs.chemrev.9b00550.

[26] S. Dalapati, M. Addicoat, S. Jin, T. Sakurai, J. Gao, H. Xu, S. Irle, S. Seki, D. Jiang, Rational design of crystalline supermicroporous covalent organic frameworks with triangular topologies, Nature Communications 6 (2015) 7786. https://doi.org/10.1038/ncomms8786.

[27] X. Feng, L. Chen, Y. Dong, D. Jiang, Porphyrin-based two-dimensional covalent organic frameworks: synchronized synthetic control of macroscopic structures and pore parameters, Chem. Commun. (Camb) 47 (2011) 1979–1981. https://doi.org/10.1039/C0CC04386A.

[28] T.-Y. Zhou, S.-Q. Xu, Q. Wen, Z.-F. Pang, X. Zhao, One-Step Construction of Two Different Kinds of Pores in a 2D Covalent Organic Framework, J. Am. Chem. Soc. 136 (2014) 15885–15888. https://doi.org/10.1021/ja5092936.

[29] S. Dalapati, S. Jin, J. Gao, Y. Xu, A. Nagai, D. Jiang, An Azine-Linked Covalent Organic Framework, J. Am. Chem. Soc. 135 (2013) 17310–17313. https://doi.org/10.1021/ja4103293.

[30] B. Wang, Hybrid metal-organic framework and covalent organic framework polymers, Royal Society of Chemistry, London, 2022.

[31] S. Wang, V.A. Reddy, M.C.-Y. Ang, J. Cui, D.T. Khong, Y. Han, S. in Loh, R. Cheerlavancha, G.P. Singh, S. Rajani, M.S. Strano, Single-Crystal 2D Covalent Organic Frameworks for Plant Biotechnology, J. Am. Chem. Soc. 145 (2023) 12155–12163. https://doi.org/10.1021/jacs.3c01783.

[32] C. Yin, M. Liu, Z. Zhang, M. Wei, X. Shi, Y. Zhang, J. Wang, Y. Wang, Perpendicular Alignment of Covalent Organic Framework (COF) Pore Channels by Solvent Vapor Annealing, J. Am. Chem. Soc. 145 (2023) 11431–11439. https://doi.org/10.1021/jacs.3c03198.

[33] M.S. Jagirani, Z.P. Gumus, M. Soylak, Covalent Organic Frameworks, a Renewable and Emergent Source for the Separation and Pre-concentration of the Traces of Targeted Species, Microchemical Journal 191 (2023) 108820. https://doi.org/10.1016/j.microc.2023.108820.

[34] L. Peng, Q. Guo, C. Song, S. Ghosh, H. Xu, L. Wang, D. Hu, L. Shi, L. Zhao, Q. Li, T. Sakurai, H. Yan, S. Seki, Y. Liu, D. Wei, Ultra-fast single-crystal polymerization of large-sized covalent organic frameworks, Nature Communications 12 (2021) 5077. https://doi.org/10.1038/s41467-021-24842-x.

[35] P.J. Waller, F. Gándara, O.M. Yaghi, Chemistry of Covalent Organic Frameworks, Acc. Chem. Res. 48 (2015) 3053–3063. https://doi.org/10.1021/acs.accounts.5b00369.

[36] F.J. Uribe-Romo, J.R. Hunt, H. Furukawa, C. Klöck, M. O'Keeffe, O.M. Yaghi, A crystalline imine-linked 3-D porous covalent organic framework, J. Am. Chem. Soc. 131 (2009) 4570–4571. https://doi.org/10.1021/ja8096256.

[37] C.-X. Yang, C. Liu, Y.-M. Cao, X.-P. Yan, Facile room-temperature solution-phase synthesis of a spherical covalent organic framework for high-resolution chromatographic separation, Chem. Commun. (Camb) 51 (2015) 12254–12257. https://doi.org/10.1039/c5cc03413b.

[38] R.E. Morris, Ionothermal synthesis--ionic liquids as functional solvents in the preparation of crystalline materials, Chem. Commun. (Camb) (2009) 2990–2998. https://doi.org/10.1039/B902611H.

[39] J. Maschita, T. Banerjee, G. Savasci, F. Haase, C. Ochsenfeld, B.V. Lotsch, Ionothermal Synthesis of Imide-Linked Covalent Organic Frameworks, Angew. Chem. Int. Ed Engl. 59 (2020) 15750–15758. https://doi.org/10.1002/anie.202007372.

[40] H. Lee, J.-U. Joo, A. Dhamija, A. Gunnam, J. Koo, P. Giri, Y. Ho Ko, I.-C. Hwang, D.-P. Kim, K. Kim, Flow Synthesis of Gigantic Porphyrinic Cages: Facile Synthesis of P12 L24 and Discovery of Kinetic Product P9 L18, Chemistry 29 (2023) e202300760. https://doi.org/10.1002/chem.202300760.

[41] M. Traxler, W.R. Dichtel, Continuous flow synthesis and post-synthetic conversion of single-crystalline covalent organic frameworks, Chem. Sci. 15 (2024) 7545–7551. https://doi.org/10.1039/D4SC01128G.

[42] Dipl.- Ing. Michael König, COF chemical reaction equation.

[43] F. Zhang, Y. Wang, H. Zhao, X. Dong, X.-K. Gu, X. Lang, Expanding Olefin-Linked Covalent Organic Frameworks toward Selective Photocatalytic Oxidation of Organic Sulfides, ACS Applied Materials & Interfaces 16 (2024) 8772–8782. https://doi.org/10.1021/acsami.3c16838.

[44] O. Levenspiel, Chemical Reaction Engineering, Wiley, 1999.

[45] B. Scarlett, S. Lowell, J.E. Shields, M.A. Thomas, M. Thommes, Characterization of Porous Solids and Powders: Surface Area, Pore Size and Density, Springer Netherlands, Dordrecht, 2004.

[46] S. Brunauer, P.H. Emmett, E. Teller, Adsorption of gases in multimolecular layers, J. Am. Chem. Soc. 60 (1938) 309–319.

[47] M. Thommes, K. Kaneko, A.V. Neimark, J.P. Olivier, F. Rodriguez-Reinoso, J. Rouquerol, K.S. Sing, Physisorption of gases, with special reference to the evaluation of surface area and pore size distribution (IUPAC Technical Report), Pure and Applied Chemistry 87 (2015) 1051–1069. https://doi.org/10.1515/pac-2014-1117.

[48] A. Uthaman, S. Thomas, T. Li, H. Maria, Advanced Functional Porous Materials, Springer International Publishing, Cham, 2022.

[49] I. Langmuir, THE CONSTITUTION AND FUNDAMENTAL PROPERTIES OF SOLIDS AND LIQUIDS. PART I. SOLIDS, J. Am. Chem. Soc. 38 (1916) 2221–2295. https://doi.org/10.1021/ja02268a002.

[50] A.B. N. Hwang, BET Surface Area Analysis of Nanoparticles. OpenStax-CNX module: m38278 1, OpenStax-CNX (2011).

[51] B.C. Smith, Fundamentals of Fourier transform infrared spectroscopy, secondnd ed (Online-Ausg.), CRC Press, Boca Raton, Fla, 2011.

[52] A.F. Craievich, Synchrotron SAXS Studies of Nanostructured Materials and Colloidal Solutions: A Review, Mat. Res. 5 (2002) 1–11. https://doi.org/10.1590/S1516-14392002000100002.

[53] I.W. Hamley, Small-Angle Scattering, Wiley, 2021.

[54] E. Walenta, Small angle x-ray scattering. Von O. G LATTER und O. K RATKY London: Academic Press Inc. Ltd. 1982. ISBN 0-12-286280-5. X, 515 Seiten, geb. £ 43,60; US $ 81.00, Acta Polymerica 36 (1985) 296. https://doi.org/10.1002/actp.1985.010360520.

[55] H. Satha, I. Kouadri, D. Benachour, Thermal, Structural and Morphological Studies of Cellulose and Cellulose Nanofibers Extracted from Bitter Watermelon of the Cucurbitaceae Family, J Polym Environ 28 (2020) 1914–1920. https://doi.org/10.1007/s10924-020-01735-6.

[56] E. Smith, G. Dent, Modern Raman Spectroscopy – A Practical Approach, Wiley, 2004.

[57] John R. Ferraro, Kazuo Nakamoto and Chris W. Brown, Introductory Raman Spectroscopy, Elsevier, 2003.

[58] J.C. George Turrell, Raman Microscopy, Elsevier, 1996.

[59] Technobis, Crystalline. https://www.crystallizationsystems.com/products/crystalline/.

[60] Kaiser, Raman. https://www.at.endress.com/de/messgeraete-fuer-die-prozesstechnik/optische-analyse-produktuebersicht/raman-rxn2-analysensystem?t.tabId=product-overview.

[61] Lamda, Spritzenpume. https://www.lambda-instruments.com/de/spritzenpumpe/.

[62] Langraf, Spritzenpumpe. https://www.hll.de/12/1/VP223/106720120/106720120%20VGKL+Seite.html.

[63] HiTEC ZANG, SyrDos. https://www.hitec-zang.de/de/produkte-loesungen/dosiersysteme-pumpen/spritzenpumpen/.

[64] Phrozen, Sonic Mini 8K S. https://phrozen3d.com/pages/sonic-mini-8k-s.

[65] Phrozen, Aqua 3D Printing Resin Oat White. https://phrozen3d.com/products/aqua-resin?_pos=1&_psq=oat+&_ss=e&_v=1.0&variant=45736395931835.

[66] Phrozen, TR250LV High Temp 3D Printing Resin Gray. https://phrozen3d.com/products/tr250lv-high-temp-resin?_pos=1&_psq=high+temp&_ss=e&_v=1.0.

[67] C.H. Feriante, S. Jhulki, A.M. Evans, R.R. Dasari, K. Slicker, W.R. Dichtel, S.R. Marder, Rapid Synthesis of High Surface Area Imine-Linked 2D Covalent Organic Frameworks by Avoiding Pore Collapse During Isolation, Adv. Mater. 32 (2020) e1905776. https://doi.org/10.1002/adma.201905776.

[68] Michael Radl, Preliminary Experiments for the Development of Continuous Covalent Organic Frameworks Synthesis: Construction Thesis.

[69] S.T. Emmerling, L.S. Germann, P.A. Julien, I. Moudrakovski, M. Etter, T. Friščić, R.E. Dinnebier, B.V. Lotsch, In situ monitoring of mechanochemical covalent organic framework formation reveals templating effect of liquid additive, Chem 7 (2021) 1639–1652. https://doi.org/10.1016/j.chempr.2021.04.012.

This thesis was reviewed and edited using Grammarly and other AI tools.